MAX-PLANCK-GESELLSCHAFT

Phys.Chem.Chem.Phys. 9 (2007) 3600-3618

Activation and isomerization of n-butane on sulfated zirconia model systems - An integrated study across the materials and pressure gaps

C. Breitkopf,[a] H. Papp,[a] X. Li,[b] R. Olindo,[b] J.A. Lercher,[b] R. Lloyd,[c] S. Wrabetz,[c] F.C. Jentoft,[c] K. Meinel,[d] S. Förster,[d] K.-M. Schindler,[d] H. Neddermeyer,[d] W. Widdra,[d] A. Hofmann[e], J. Sauer[e]

[a] Universität Leipzig, Institut für Technische Chemie, Linnéstraße 3, 04103 Leipzig, Germany
[b] Technische Universität München, Lehrstuhl für Technische ChemieII, , 85747 Garching, Germany
[c] Fritz Haber Institute of the Max Planck Society, Faradayweg 4-6,14195 Berlin, Germany
[d] Martin-Luther-University Halle-Wittenberg, Institute of Physics, 06099 Halle, Germany
[e] Institut für Chemie, Humboldt-Universität zu Berlin, D-10099 Berlin, Germany

Received 6th February 2007, Accepted 11th May 2007
First published as an Advance Article on the web 1st June 2007

Abstract

Butane activation has been studied using three types of sulfated zirconia materials, single-crystalline epitaxial films, nanocrystalline films, and powders. A surface phase diagram of zirconia in interaction with SO_3 and water was established by DFT calculations which was verified by LEED investigations on single-crystalline films and by IR spectroscopy on powders. At high sulfate surface densities a pyrosulfate species is the prevailing structure in the dehydrated state; if such species are absent, the materials are inactive. Theory and experiment show that the pyrosulfate can react with butane to give butene, H_2O and SO_2, hence butane can be activated via oxidative dehydrogenation. This reaction occurred on all investigated materials; however, isomerization could only be proven for powders. Transient and equilibrium adsorption measurements in a wide pressure and temperature range (isobars measured via UPS on nanocrystalline films, microcalorimetry and temporal analysis of products measurements on powders) show weak and reversible interaction of butane with a majority of sites but reactive interaction with < 5 μmol/g sites. Consistently, the catalysts could be poisoned by adding sodium to the surface in a ratio S/Na=35. Future research will have to clarify what distinguishes these few sites.

1. Introduction

The isomerization of *n*-alkanes is an important technical conversion to increase the fraction of branched components in the feedstock. Bifunctional catalytic materials like such as Pt-zeolites or chlorinated aluminas with Pt are state of the art.[1] Still, less corrosive catalysts, which are able to isomerize light alkanes at low temperatures, are highly desirable. In this respect, sulfated zirconias (SZ) modified with noble metals offered the possibility of an active catalyst system applicable at moderate temperature conditions.

Already in 1962, Holm and Bailey[2] described the potential of SZ in the isomerization of *n*-butane. However, it was the work of Hino and Arata[3,4] that became the starting point of an extensive research in this field. Since that time, numerous papers were published focusing on selected aspects like such as preparation,[5,6,7,8] the crystal phases of zirconia,[9,10] the kind of sulfation agent like ammonium sulfate[11] or gaseous SO_2/SO_3,[12] the effect of the calcination procedure on the catalytic activity,[13,14] the surface composition,[15,16] and the role of acidic properties[17,18,19,20] to give only a selection.

Despite this intensive research over the last two decades, a consistent model regarding the nature of the sites responsible for activation and conversion of alkanes only emerged over the last years. Correlations between zirconia bulk and sulfate surface structures have been rudimentary, and it is unknown, e.g., how the sulfate coordination alters the acidic or oxidizing properties of the material. Such correlations are difficult to establish from the existing literature because of the wide variety of preparation methods used and problems reported with respect to catalyst reproducibility,[7,21] including the general heterogeneity of a typi-

cal powder catalyst. Missing data on surface structural details hampered the comparison of theoretical and experimental work.

An approach that has not been pursued, however, in elucidating structure and function of SZ is the use of model systems in combination with surface analytical techniques and theory. Such an integrated study is presented in the following. Three types of SZ models ranging from single-crystalline epitaxial films, via nanocrystalline films to optimized powders have been developed. Systems of reduced complexity, as models are, do not necessarily exhibit the same functionalities as the catalyst of interest. Hence, it has to be ensured that no such "materials gap" exists and that reactive specimens have been obtained. Furthermore, surface science methods require ultra high vacuum conditions (UHV), whereas typical catalyst operating pressures range from atmosphere to several bar. To verify that a "pressure gap" is absent and results are transferable despite varying conditions, analytical methods covering a wide pressure range were selected.

A model for SZ with a well-defined surface has been obtained by epitaxial growth of single-crystalline zirconia films on Pt(111). This single-crystalline film approach also allowed the application of surface sensitive tools using electrons such as scanning tunneling microscopy (STM), low energy electron diffraction (LEED), and Auger electron spectroscopy (AES). These methods are in general not applicable to insulating bulk oxides due to charging effects. However, charge accumulation can be avoided by investigating thin film samples prepared on conducting substrates, as has been demonstrated for other insulating oxides.[22] To bridge to the zirconia powders and to still be able to apply surface science techniques without compromising the chemical complexity of SZ, additionally a nanocrystalline SZ thin film model system has been prepared by a wet-chemical route. The nanocrystalline thin film preparation is designed to mimic the powder synthesis route as closely as possible. The conducting and non-porous properties of these films also allow characterization by techniques whose application is either not possible or severely hindered on powders. Powder samples of an active material, on the other hand, are used as models closest to a real catalyst allowing reaction studies conducted under realistic conditions and at high conversions. Powder samples with different sulfate surface densities were prepared carefully varying the sulfation route.

Theoretical investigations targeted not only the identification of stable surface structures, their acidic properties, and reactivity, but also the mechanism of *n*-butane activation. The reactivity of the prepared systems was experimentally studied with *n*-butane as a reactant, the partial pressure was varied by ten orders of magnitude, and static equilibrium adsorption, continuous flow and transient experiments were applied.

This concerted study yielded the following main results: (i) a pyrosulfate surface structure, identified as the prevailing species after typical activation, initiates *n*-butane conversion via an oxidative dehydrogenation step, (ii) the number of acid sites that protonate the observed unsaturated hydrocarbon species (the dehydrogenation product) is estimated and identified as minority species, and (iii) a kinetic model consistent with catalytic performance data is established.

2. Experimental and theoretical methods

2.1. Preparation and characterization of single-crystalline films

For preparing single crystalline zirconia films, a Pt(111) single crystal has been used as substrate. The preparation follows a procedure described by Maurice et al.[23] who presented first studies on well-ordered ZrO_2 films on metals. Experience gained from preparation of well-defined films of other metal oxides[24,25,26,27] has also been employed to optimize the structural order of the ZrO_2 films.

The experiments were performed in an UHV chamber equipped with facilities for STM, LEED, AES, defined inlet of gases, and Zr evaporation. Further details are described elsewhere.[28,29] Briefly, the Pt(111) substrate was cleaned in situ by cycles of Ar ion bombardment, UHV heating, and heating in O_2 atmosphere.[30] The single-crystalline ZrO_2 films have been prepared by reactive deposition of Zr in an O_2 atmosphere (pressure 10^{-6} hPa) on Pt(111) at a temperature of 470 K. Afterwards, the film structure was optimized by post-annealing in O_2 atmosphere at temperatures up to 1000 K.[28,29] Zr was evaporated from the tip of a Zr rod heated by electron bombardment. The growth rate of the zirconia films was about 0.1 monolayers (ML) per minute. For film sulfation, SO_3 gas was used following the findings on polycrystalline SZ.[38] In order to increase the dosing efficiency, a pipe-like SO_3 doser was implemented which increases the local SO_3 pressure at the sample by a factor of 100 and allows dosage at relatively low background pressure in the chamber.[31] After preparation, the morphology, structure, and composition of the films have been characterized using a home-built STM,[24] a high-resolution LEED system for spot profile analysis (SPA-LEED), and a cylindrical mirror analyzer for AES.

2.2. Preparation and characterization of nanocrystalline films

The synthesis route outlined here has been adapted from ref.[32] and was further developed to yield smooth, non-porous, continuous, nanocrystalline SZ thin films.[33] Briefly, single-crystalline Si(100) wafers were used as substrate, and were first cleaned and oxidized. To form the self-assembled monolayer (SAM), a prerequisite to deposit continuous thin films,[34] the wafers were immersed in a solution of 1-thioacetato-16-(trichlorosilyl)hexadecane. The hydrophobic terminal thioacetate group of the SAM was then oxidized using a solution of $KHSO_5$*$KHSO_4$*K_2SO_4

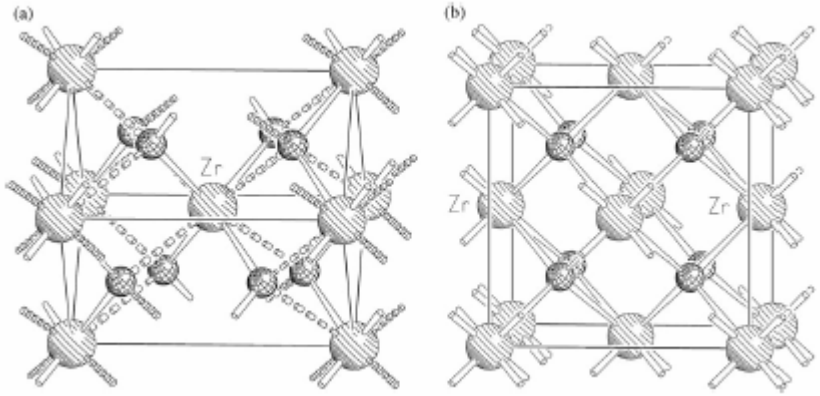

Figure 1: The tetragonal (left) and cubic (right) zirconia unit cell. The (calculated) bond lengths are 210 (full) and 243 pm (dashed) for t-ZrO_2 and 223 pm for c-ZrO_2. The t-ZrO_2 cell is rotated by 45° along c for better comparison.

to the desired sulfonic acid group, which is necessary for film deposition via heterogeneous nucleation. The wafers were then heated slowly (at ~1 K/min, in order to avoid homogeneous precipitation[35]) to 323 K in an aqueous solution of 4 mM zirconium (IV) sulfate tetrahydrate in 0.4 M hydrochloric acid ("as deposited" films). The film thickness can be accurately controlled by the deposition time; a linear growth rate of approximately 1 nm/h has been observed for 2 to 192 h depositions.[36] Films were prepared with various thicknesses in order to suit the different characterization techniques employed; thinner films to maximize the conductivity of the samples and thicker to minimize substrate contributions in the spectra. Thermal treatment of the nanocrystalline films was performed in an inert atmosphere (to avoid potential heat damage to the film from combustion of the SAM) or in air (to mimic the powder preparation). The films were heated to 823 K for 2 h. The nanocrystalline films were characterized using atomic force microscopy (AFM), scanning and transmission electron microscopy (SEM and TEM), thermal desorption spectroscopy (TDS) of ammonia, ultraviolet and X-ray photoelectron spectroscopy (UPS and XPS), and near edge X-ray absorption fine structure spectroscopy (NEXAFS).

2.3. Preparation and characterization of powders

Powders for the catalytic studies were prepared (i) by a standard precipitation technique[37] or (ii) by calcining a commercially available zirconium hydroxide precursor.

For method (i), the zirconium hydroxide was precipitated from zirconyl nitrate with ammonia at pH 8.4 and the precipitate was aged either 1 h at room temperature (RT) or 24 h at 373 K in the mother liquor. The products were sulfated using ammonium sulfate to achieve an optimum amount of sulfate on the surface corresponding to monolayer coverage. The materials were calcined at 873 K for 3 h in air and are referred to as cat1 (short aging at RT) and cat2. The detailed preparation of these catalysts is described elsewhere[72] Due to the different aging procedures, both catalysts developed different specific surface areas. As both hydrous zirconias were treated with the same sulfate amount, two powder model systems with different sulfur site densities were obtained.

The parent reference sample (ii), hereafter sz-mel, was obtained by calcination at 873 K of a sulfated zirconium hydroxide (MEL Magnesium Electron, Inc. XZO 1077/01)[38]. First, sz-mel was suspended in bi-distilled water, yielding the water-washed sample. Subsequently, this washed sample was treated with gaseous SO_3 following a newly developed sulfation procedure.[38]

Powder samples were characterized by XRD, XPS, N_2-adsorption, diffuse reflectance infrared Fourier transform spectroscopy (DRIFTS) without and with pyridine adsorption, temperature programmed desorption (TPD) of ammonia, adsorption microcalorimetry, temporal analysis of products (TAP), and catalytic conversion of *n*-butane to *iso*-butane.

2.4. Slab models for DFT calculations

All structure optimizations have been carried out with the VASP code.[39] The standard setup is as follows: standard projector augmented waves (PAW) for core description, plane wave basis set (400 eV cutoff) and 2 Monkhorst-Pack k-points for the 6.425 • 7.284 • 30.000 $Å^3$ surface slab. The slab contains 5 'layers' of Zr_4O_8, where the bottom 3 layers are fixed to the positions of the corresponding bulk structure. More details can be found in ref. 40. The deprotonation energies have been calculated with CPMD, because VASP does not correct for charged unit cells. The optimization of the structure with the removed proton with VASP is done till Hellmann-Feynman forces are small (< 0.01 eV/Å). A single point energy calculation is carried out on this structure with CPMD. The functional and the pseudopotentials are different (CPMD: PBE/norm—conserving pseudopotential, VASP: PW91/PAW), but no large differences in energies are expected due to that approximation.

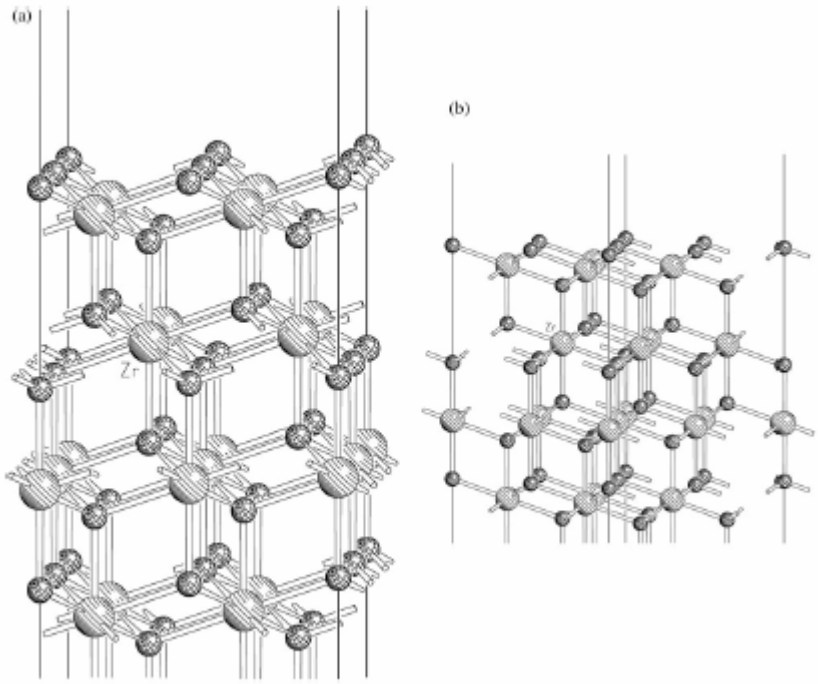

Figure 2: Four $(ZrO_2)_4$ layers of the t-ZrO_2(101) 1x2 (left) and c-ZrO_2(111) 2x2 slab (right). Long Zr—O bonds are dashed in t-ZrO_2.

3. Combined study of model systems with increasing complexity

3.1. Bulk and surface structure of zirconia – theoretical approach

Zirconia exists in three bulk modifications, the RT stable monoclinic structure (P21/c)[41], the tetragonal (P42/nmc)[42] and the cubic (Fm $\overline{3}$ m)[43] polymorph (m-, t-, c-ZrO_2; see Fig. 1). The transition temperatures are 1143 K from monoclinic to tetragonal and 2643 K from tetragonal to cubic (melting point ~2870 K). The tetragonal phase may be stabilized at RT by dopants, e.g. yttria (Y_2O_3).[44,45,46] The modification of zirconia samples with sulfate has a similar effect and stabilizes the tetragonal phase.[45] The size of the crystallites is further considered as an important parameter for the stability of t-ZrO_2 at RT (at sizes < 15 nm the tetragonal phase is preferred).[47,48]

Theory gives a more detailed picture to bulk and surface properties.[48,49,] Christensen and Carter[48] studied the surface energies of all low energy surfaces of all zirconia modifications by periodic DFT whereas Haase and Sauer[49] focused on the tetragonal phase: t-ZrO_2(101) and c-ZrO_2(111) are found most stable for the particular phases in this study (see Fig. 2). Both surfaces are non-polar and identical from the crystallographic point of view, e.g. a transfer of the t-ZrO_2 into the cubic lattice results in a small distortion of the oxygen atoms along the *c* direction of the lattice. There are then two sets of Zr—O bonds in t-ZrO_2, namely the short bonds (210 pm) and the long bonds (243 pm) instead of 223 pm for all Zr—O bonds in the c system (Fig. 3). This change in bond length decreases the unit cell volume by ~ 3%.

This property of having different metal-oxygen bond lengths appears again at the surface of t-ZrO_2. For example, the (101) surface exhibits two different Zr-atoms, one which has lost a short Zr-O bond and one which has lost a long Zr-O bond. These metal adsorption sites are henceforth considered as strong (s) and weak (w),[49] referring to the type of the lost bond and their Lewis acidity. In c-ZrO_2, all sites are identical.

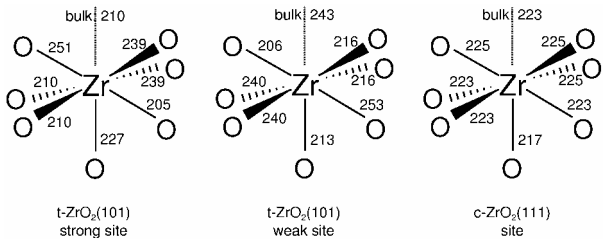

Figure 3: Three different metal sites at the t-ZrO_2(101) and c-ZrO_2(111) surface. The left zirconium atom loses a strong Zr—O bond; the middle loses a weak Zr—O bond; the right just the normal c-ZrO_2 Zr—O bond. The bulk bond lengths are 210, 243 and 223 pm for strong, weak t-Zr—O and c-Zr—O bonds, respectively.

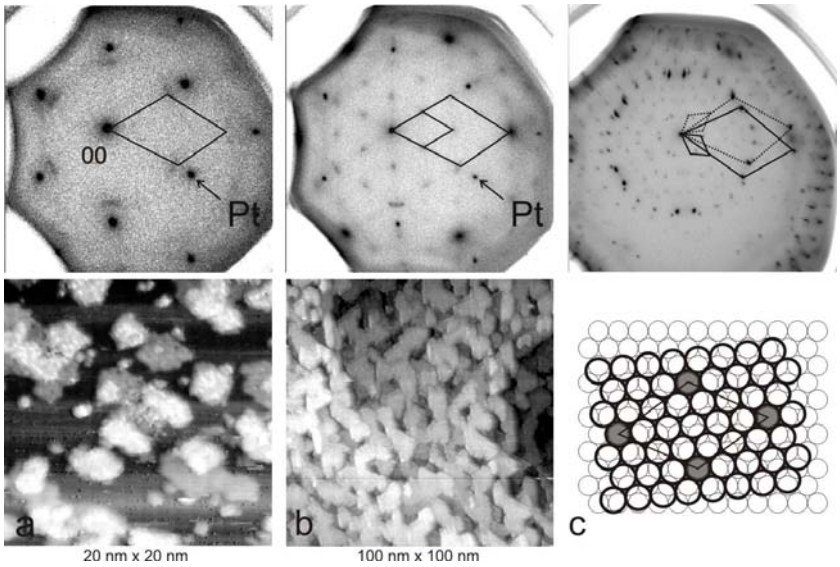

Figure 4: LEED patterns (taken at 66 eV) and STM images of ZrO_2 films on Pt(111) formed by chemical deposition of Zr in O_2 atmosphere at 470 K and post-annealing.
(a) ZrO_2 islands immediately observed after deposition (film mean thickness 0.7 ML) displaying a slightly rotated (1x1) LEED pattern (see indicated unit mesh).
(b) Continuous ZrO_2 film (film thickness 3 ML) displaying after a short 980 K post-annealing a multilayer morphology and a (2x2) structure.
(c) LEED pattern of a continuous ZrO_2 film (film thickness 5 ML) 5 min post-annealed at 980 K showing a rotated lattice (rotation angle ±6.6°, see indicated (1x1) unit meshes) with (2√3x2√3) superstructure which is commensurate to a (√19x√19)R± 36.6° superstructure at the Pt(111) interface (see small unite meshes) as visualized by a hard sphere model.

3.2. Morphology and structure of bare single-crystalline c-ZrO_2(111) films

In agreement with Maurice et al.[23], the growth of ZrO_2 on Pt(111) yields c-ZrO_2(111) films. Recently, ZrO_2(111) films have also been prepared on the (111) surfaces of Au,[50] FeO-precovered Pt,[51] and Cu.[52] Obviously, the substrate orientation is of essential importance for the crystalline nature of these films. For example using Ag(100) as the substrate only yields poly-crystalline zirconia films.[53] On Pt(111), the films grow almost unstrained in a multi-layer mode, in which two-dimensional islands are formed simultaneously one over the other (Fig. 4a). The individual layers (thickness about 0.3 nm) are formed by a Zr(111) layer sandwiched between two oxygen layers. A possible Zr surface termination as it was deduced in first studies[28] can be excluded.[29] Due to the multilayer growth mode, a hillock-like morphology develops (Fig. 4b). The interlayer diffusion is hampered during growth similar as has been found in epitaxial growth of metal films.[54] This growth mode induces an increasing surface roughness which, however, can be reduced by defined post-annealing procedures.[28]

Depending on preparation conditions and film thicknesses, different surface and interface structures develop.[55] At deposition temperatures around 470 K, the films show a (1x1) structure with a slight tendency of lattice rotation with respect to the substrate (Fig. 4a). Post-annealing of such films at temperatures around 950 K induces a slight expansion of the film lattice by about 2% and the formation of a (2x2) superstructure (Fig. 4b), which is commensurate to a (√7x√7) structure of the Pt(111) interface as has been already reported by Maurice et al.[23] and corroborated by DFT calculations.[56] Intensifying post-annealing induces a film domain rotation by 6.6 ° with respect to the Pt(111) lattice. In addition, the film lattice is slightly compressed by about 3 %. Under such conditions, a (2√3x2√3) superstructure is established, which is commensurate to a (√19x√19)R± 36.6° superstructure of the Pt(111) interface (Fig. 4c). Besides these structures, a non-rotated (4x4) superstructure has been found for submonolayer films at temperatures around 980 K. In addition to that, a non-commensurate $Zr_xO_yPt_z$ intermixing phase has been observed at temperatures above 1250 K. All ZrO_2 structures have been imaged with STM. Atomic resolution was obtained for the (1x1) and (2x2) structures (see refs. 28 and 55).

3.3. Sulfation

Zirconia can be sulfated *via* liquid or gas phase reactions. In liquid phase, generally ammonium sulfate but also sulfuric acid are applied as sulfation agents. It could be shown that use of ammonium sulfate is superior, as it appears the most effective agent to give the highest nominal sulfur content compared to sulfuric acid.[1] Other

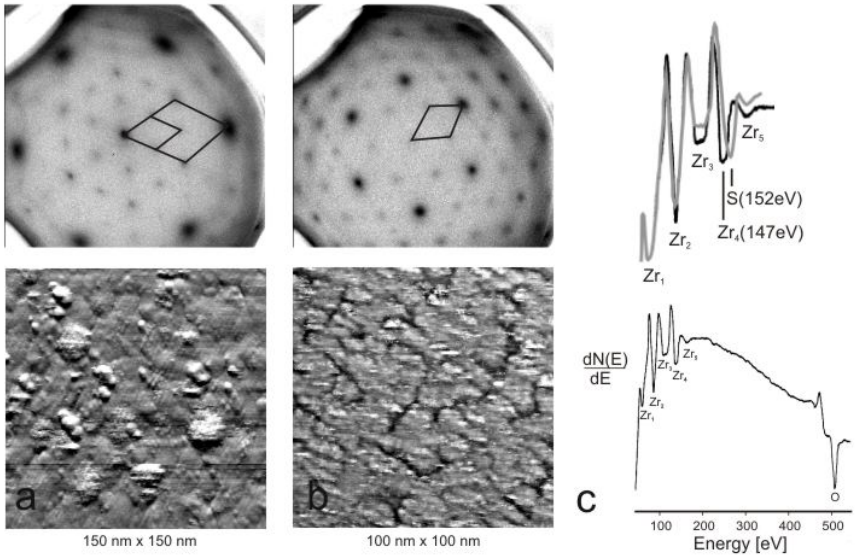

Figure 5: LEED patterns, STM images and AES spectra of a 10 ML thick continuous ZrO_2 film taken before (a) and after (b) SO_3 exposure at RT up to saturation (50000 L). The corresponding AES spectra are shown in (c) in black and gray, respectively. During sulfation, the initial (2x2) superstructure is outshined by the (√3x√3)R30° sulfation structure (see indicated unit meshes). In AES spectra (c), the SO_3 interaction is indicated by a slight shift of the Zr(147eV) peak to the Si(152eV) peak position.

drawbacks of sulfuric acid sulfation were shown to be its strong interaction with the surface of the bulk zirconia which caused spontaneous formation of isolated sulfates,[57] and the formation of the monoclinic phase of zirconia.[58] Application of a surplus of sulfation agent either by ammonium sulfate or sulfuric acid led to the loss of labile sulfates during thermal activation[59] and hindered the formation of well-crystallized materials.[60] For all sulfation agents it has been proven that an optimal amount of sulfate coverage exists, e.g., a surplus of sulfate is generally removed by calcination.[1] Beside sulfates, also persulfates[61] have been used as sulfation agents to induce bridged sulfate structures on the surface, but no positive effect on the catalytic activity was observed. Other sulfation techniques made use of gaseous sulfur-sources like SO_2/O_2.[12,62] Sulfated zirconia can also be produced by thermal decomposition of zirconium sulfate.[63]

In this study, all model systems were sulfated using either gaseous SO_3 or ammonium sulfate or in case of the nanocrystalline films, the sulfates were introduced via the precursor zirconium sulfate. The single-crystal ZrO_2 films were sulfated with gaseous SO_3 following the preparation of the powder models (see chapter 3.3.2) which resulted in active catalysts.[38]

3.3.1. Sulfation of single-crystalline ZrO_2 film surfaces with SO_3

For the sulfation and reaction studies, ZrO_2 films with a minimum thickness of 10 ML were used, which completely covered the substrate. Hence, any influence of bare metallic Pt could be excluded. In addition to that, preparation conditions were selected such that the films developed a bright and simple (2x2) superstructure in order to facilitate interpretation. Fig. 5a shows the LEED pattern and the STM image of such a 10 ML thick film. Due to the relatively large film thickness, no Pt spots are visible in the LEED pattern, contrary to the film shown in Fig. 4b. The large film thickness, however, hampered high-resolution STM imaging and only large scale overview inspections were possible. However, they clearly demonstrate the film continuity as can be seen in Fig. 5a.

Fig. 5b shows the film after sulfation. A SO_3 exposure at RT (local pressure $5x10^{-4}$ hPa) was applied until a surface saturation was reached at about $5x10^4$ Langmuir (L). The LEED pattern revealed the formation of a specific SO_3-induced sulfation structure. As indicated by the unit mesh, a clear (√3x√3)R30° pattern is induced (ref. 31). During SO_3 exposure, tiny channels developed on the film surface (appearing as darker lines in the STM image of Fig. 5b), the origin of which is unknown. They reach, however, only a depth of 2-3 ML and do not destroy the film continuity. In Fig. 5c, AES spectra of the clean (black) and the SO_3-saturated ZrO_2 film surface with the (√3x√3)R30° structure (gray) are shown. Several Zr Auger peaks are observed at 33, 92, 124, and 147 eV (labeled Zr_1-Zr_5) and an O peak at 510 eV. The SO_3 uptake is indicated by a change of the I_{Zr}/I_O Auger intensity ratios mainly caused by the SO_3-induced attenuation of the Zr Auger electrons. The SO_3 uptake also leads to a slight shift of the Zr_4 peak minimum from 147 eV to 152 eV, which coincides with the minimum of the S Auger peak. An estimation of the surface composition yielded a minimum S coverage of 0.15 with respect to $ZrO_2(111)$.[31] Annealing the sample in UHV revealed that the (√3x√3)R30° sulfation structure is stable up

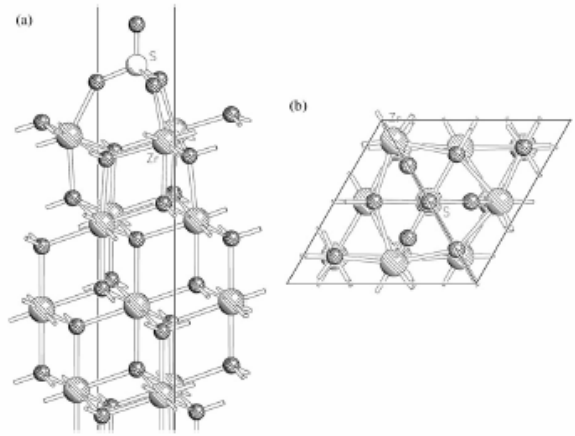

Figure 6: Arrangement of S, O and Zr atoms of the (√3x√3)R30°-SO_3-ZrO_2(111) structure as determined by DFT

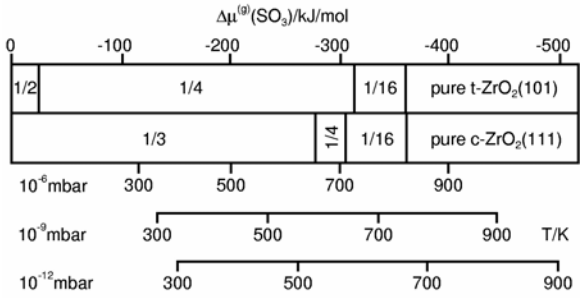

Figure 7: Comparison of the most stable sulfated cubic ZrO_2(111) and tetragonal ZrO_2(101) surfaces. For the relation of coverage Θ, superstructure and number of surface Zr atoms compare with text.

to temperatures of about 650 K. At about 700 K, the (√3x√3)R30° structure gradually disappeared and the LEED spots of the initial (2x2) structure reappeared.[31]

DFT calculations of SO_3 adsorbed on c-ZrO_2(111) confirm this interpretation.[31] The most stable high pressure structure at an SO_3 coverage of 1/3 is the (√3x√3)R30°-SO_3-ZrO_2(111) structure (Fig. 6). Other coverages like 1/4 and 1/2 are also considered and may appear at reduced SO_3 pressures (Fig. 7). The (4x4) structure with coverage of 1/16 is the model for weakly interacting adsorbates.

The adsorption energy of the experimentally observed (√3x√3)R30°-SO_3-c-ZrO_2(111) structure is -307 kJ/mol at a coverage of 1/3. The only bond distance changing significantly is d(SO–Zr) = 212 pm . Two oxygen atoms of the SO_3 molecule bind to one Zr atom each, whereas one oxygen of the zirconia surface moves towards sulfur in a way that the S atom becomes fourfold coordinated. The third bond is extended to a surface oxygen atom, which loses its bonds to the two Zr atoms, to which SO_3 oxygen atoms are attached. The O atom moves rather far towards the sulfur. All Zr atoms connected to S via Zr—O—S bonds retain their seven-fold coordination. For coverages of e.g. 1/3 or 1/9, structures are strictly symmetry equivalent (C_3 axis).

Fig. 7 shows the Gibbs free energy of SO_3 adsorption as a function of the relative chemical potential of SO_3, $\Delta\mu_{SO_3}^{(g)}$. For a given SO_3 partial pressure, $\Delta\mu$ translates into a temperature. Temperature scales are given for three different experimentally relevant pressures, $p(SO_3)$. In agreement with experiment, Fig. 7 shows that the observed (□3x□3)R30° structure appeared to have the most negative Gibbs free energy of adsorption for low temperature, and, hence, is most stable. Fig. 7 also predicts that with increasing temperature there is a small range in which the (2x2) structure (Θ=1/4) and the (4x4) structure (Θ=1/16) should be most stable before all SO_3 desorbs and the bare ZrO_2 surface is obtained.

The crystallographic orientations of the c-ZrO_2(111) and t-ZrO_2(101) surfaces are different, but the structure of the surfaces is quite similar. This originates from the structures of the systems: t-ZrO_2 differs from c-ZrO_2 by a slight displacement of the oxygen atoms in the unit cell away from the high symmetry positions. At the ideal high symmetry positions, the crystal structure would be the fluorite type of c-ZrO_2. The slight displacement leads to two different Zr atoms at the surface, where one has lost a strong (210 pm, *(s)*) Zr–O bond, the other a weak (243 pm, *(w)*) Zr–O bond.[42] The t-ZrO_2(101) surface is always rectangular and contains at least two Zr surface atoms that are different. Chemically, these two surfaces differ in the average bond length and the tiny buckling of the oxygen atoms. The (√3x√3)R30° or other structures with Θ = 1/3 do not exist on the t-ZrO_2(101) surface due to symmetry reasons. The adsorption energies of SO_3 on c-ZrO_2(111) may be compared with the t-ZrO_2(101) average adsorption energies on the strong (s) and weak (w) adsorption sites. Starting at low coverage (1/16), an average adsorption energy of -303 kJ/mol for t-ZrO_2 is obtained, which is higher than the corresponding value for the cubic system (-364 kJ/mol). This trend continues for lower coverages Θ = ¼ and Θ = ½, but is less pronounced (Θ = ¼: -317 vs. -298 kJ/mol and Θ = ½: -189 vs. -181 kJ/mol), for cubic vs. tetragonal, respectively.

The different adsorption behavior on c-ZrO_2(111) and t-ZrO_2(101) may originate from the different average Zr—O bond lengths in cubic and tetragonal zirconia (relation 1:1.023) and therefore the different Lewis acidity of the Zr atoms.[64] In Fig. 7, stability plots for c-ZrO_2 and t-ZrO_2 are compared in a simplified way. The surface unit cell of t-ZrO_2(101) is twice as large as the surface unit cell of c-ZrO_2(111). Therefore, different periodicities for the same coverage can be observed. The reason why there is no Θ = 1/3 for t-ZrO_2(101) is symmetry, as outlined above. So Θ = 1/4 is the prevailing coverage for the tetragonal surface, in contrast to the prevailing (√3x√3)R30° adsorption structure for cubic zirconia at Θ = 1/3. The difference in adsorption energies of the prevailing SO_3 structures results

Table 1: Sulfate content, XRD, acid site distribution (pyridine adsorption), and catalytic activity of SO_3 treated and water washed powder samples

Sample	Sulfate content SO_4^{2-}/mmol g^{-1}	t-phase (%) (XRD)	Acid sites/mmol g^{-1} (pyridine adsorption)		Maximum catalytic activity/ $\times 10^2$ μmol g^{-1} s^{-1}
			Brønsted	Lewis	
sz-mel	0.44	100	0.050	0.106	1.7
sz-mel water washed	0.25	58	0	0.163	0.0
sz-mel water washed + SO_3-treated	0.91	58	0.113	0.054	13.0
pure zirconia SO_3-treated[a]	1.15	30	0.173	0.089	5.5

[a] Not discussed in the paper, (see ref. 124).

in earlier disappearance of the (√3x√3)R30° type at high temperature or low pressure. The low coverage structures at the transition to pure zirconia may also be a model for disordered adsorption. Unfortunately, this coverage range is not yet accessible in present experiments.

3.3.2 Sulfation of powders with SO_3

Powders were sulfated with SO_3 to demonstrate that active catalysts can be obtained in this way. Indeed, such samples exhibited activity in low temperature *n*-butane isomerization comparable to that of conventionally sulfated ZrO_2 (Table 1). Furthermore, with this method active samples were obtained independent of the initial crystallographic phase of zirconia (monoclinic/tetragonal). After sulfation with gaseous SO_3, zirconia with high monoclinic content showed a catalytic activity corresponding to that of tetragonal sulfated zirconia. This contradicts the widely publicized statement that, to induce a high catalytic activity, sulfation must be performed on an amorphous zirconium hydroxide or on tetragonal or cubic zirconia.[65,66] Moreover, this sulfation method can be applied also to already sulfated and active samples. In this case, SO_3 treatment drastically enhances the catalytic activity up to one order of magnitude. Finally, beside the practical advantages and its successful application to a broad variety of zirconia substrates, this sulfation method helped in clarifying the real function of the final calcination step involved in the classical preparation procedure of sulfated zirconia,[67] the nature of the active sites,[62] and the correlation existing between crystalline phase, sulfate uptake, and catalytic activity.[38] It should be noted that, after sulfation with gaseous SO_3, the calcination step at high temperature, which is required after sulfation with liquid agent, is not necessary.

3.3.3. Sulfated zirconia nanocrystalline films via thermal decomposition of zirconium sulfate

For creating sulfated nanocrystalline films, the preparation route based on the thermal decomposition of zirconium sulfate was used. First, zirconium and sulfate are deposited on the SAM-modified substrate followed by thermal treatment. AFM and SEM investigations[33] have revealed the surfaces of the films to be flat and crack free after thermal treatment in argon or air. Cross section TEM,

Table 2: XPS quantification of surface composition of 24 h deposited films on a 750 μm thick Si substrate in comparison to powder catalyst cat1. Note: Oxygen content of films has contribution from the silica layer.

At%	Zr	O	S
As deposited	14.5	79.3	6.2
Air 823 K	18.4	77.6	3.9
Nitrogen 823 K	25.1	74.9	n.d.
Powder	26	67	6.8

of the as deposited films has shown the zirconia precursor layer to be continuous and of homogeneous thickness.[34] Electron diffraction patterns of the films thermally treated in argon demonstrated that below 798 K the structure does not change from the amorphous state, whereas above 823 K crystallization of the zirconia to the tetragonal state occurs and above 873 K a small amount of monoclinic zirconia is seen. High resolution TEM (HRTEM) images show the 823 K argon treatment produces a continuous polycrystalline zirconia film, thinner than the as-deposited film by 60–70%, with 10–50 nm grain sizes.[36]

The surface of the nanocrystalline thin films was investigated by XPS using Mg Kα excitation (hν = 1256.3 eV). A Shirley background was subtracted and binding energies were corrected to Zr $3d_{5/2}$ = 182.2 eV of ZrO_2.[68] Atomic sensitivity factors for Zr 3d, O 1s, and S 2p were taken from ref.69. The chemical compositions of the thin films changed during thermal treatment (Table 2). The shape of the O 1s signal indicates at least two components - one at 532.0 eV attributed to sulfate and hydroxyl groups and one at 530.2 eV due to the oxide (Fig. 8). The relative intensity of the high binding energy species decreased during thermal treatment in air, concurrently the S content was reduced. Treatment in N_2 diminished the high binding energy oxygen species more than heating in air, and concomitantly, the sulfur concentration decreased below the detection level. Sulfate is less stable in inert gas than in air, which is explainable by its decomposition pathway into SO_2 (g) + ½ O_2 (g). Estimation of the thickness of the thermally treated films from the intensity of the Si 2p signal yielded typical values of 3–10 nm, depending on deposition time.[70] The results are summarized in Table 2. A main prerequisite for the prepared systems to be suitable models is that their surface chemistry should match that of typical powder catalysts, which is confirmed by the data in Table 2.

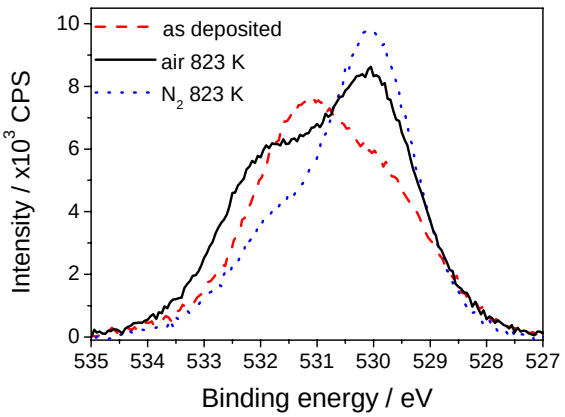

Figure 8: O 1s XP spectra of 24 h deposited films on a 750 µm thick Si substrate, as deposited and after N_2 or air treatment at 823 K.

3.3.4. Sulfation of powders by ammonium sulfate

To prepare active powder catalyst materials with reproducible properties, a standard sulfation preparation with ammonium sulfate was used.[71,72] All samples were calcined just prior to use for characterization and catalytic tests as a strong dependence of the activity and the surface properties from the storage time was found.[73,74]

Two model catalysts (cat1, cat2) with similar sulfate contents but different specific surface areas were prepared (see ref. 72). Details of the characterization by standard techniques are summarized in Table 3. The samples exhibited a different site density, which was calculated by assuming that one sulfate group covers an area of 0.25 nm.[75] A monolayer of sulfate would correspond to a site density of 4 S/nm^2. This value compares very well with adsorbed pyrosulfate from theory (DFT simulation: 4.3 S/nm^2). Therefore, it can be concluded that only cat1 showed average monolayer coverage. It was now of interest, how these textural properties influence the catalytic activity for *n*-butane isomerization at 423 K.[74] Fig. 9 shows the yield of *iso*-butane at 423 K with 5 % *n*-butane in 20 ml/min N_2. The initial rate produced by cat1 was 632 µmol/(g*h) whereas cat2 exhibited no activity in the beginning. The final rates were 425 and 114 µmol/(g*h) for cat1 and cat2, respectively. As the overall sulfate content was the same for both catalysts, the origin of the significantly different catalytic activity must arise from the sulfur site density and the possibility of various arrangements of the surface sulfates.

Table 3: XRD, N_2-adsorption, elementary analysis for powder model catalysts cat1 and cat2

	XRD	Specific surface area/m^2 g^{-1}	Pore diameter/ nm	Sulfur content/ wt%	S-atom/S nm^{-2}
cat1	Tetragonal	102	3.5	3	5.5
cat2	Tetragonal	152	4.0	3	3.7

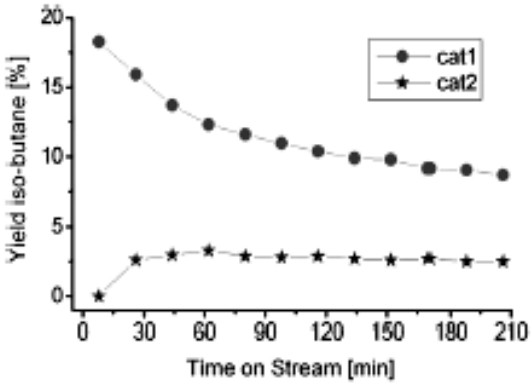

Figure 9: Comparison of the catalytic activity of sulfated zirconia catalysts cat1 and cat2 with different site densities

3.3.5. Sulfate structure

The elucidation of the prevailing structure of the sulfate group on the surface of the bulk zirconia was a field of controversial discussions, but could be clarified in the meantime.[40,62] DFT structure optimizations and statistical thermodynamics have been applied and could show that certain sulfate structures are more stable than others.[40] Several different structures and stabilities of surface species reflecting an increasing load of H_2SO_4 or SO_3 and H_2O adsorbed on the (101) surface of t-ZrO_2 were calculated. For a given composition, different "isomeric" surface structures are examined and their stabilities compared. For example, H_2O can dissociate on the surface into H^+ and OH^- and form a bridging and a terminal hydroxyl group. The surface composition is written in brackets, e.g., [SO_3,OH^-,H^+,H_2O] denotes a surface phase with one SO_3 and two H_2O molecules adsorbed on a 1x2 t-ZrO_2(101) surface cell. One of the two water molecules is dissociatively adsorbed. The surface phase [SO_4^{2-},OH^-,$3H^+$] has the same total composition, one SO_3 and two H_2O molecules on the surface, but $SO_3 \cdot H_2O$ is present as H_2SO_4 which is dissociatively adsorbed as SO_4^{2-}, $2H^+$ and the second H_2O molecule is also dissociatively adsorbed.

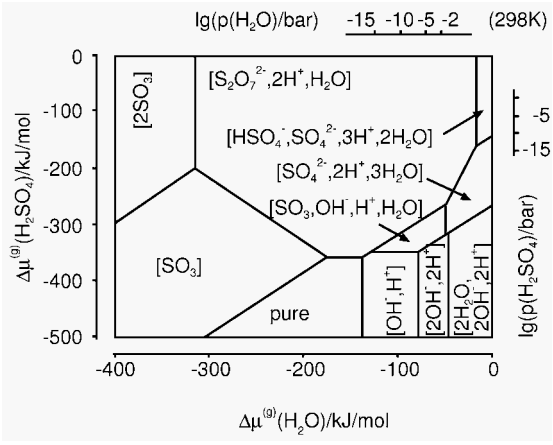

Figure 10: Surface phase diagram for the sulfated t-ZrO_2(101) surface as a function of the chemical potential of H_2SO_4 at 298K. The pressure is drawn in a logarithmic scale.

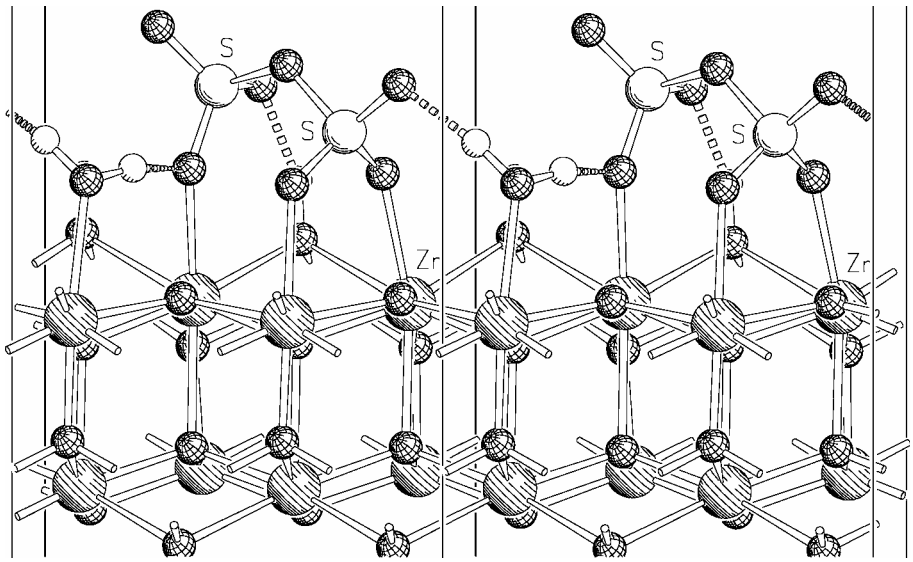

Figure 11: The $[S_2O_7^{2+},2H^+,H_2O]$ structure as calculated. One Proton is hidden behind the water molecule. Two cells are shown.

The relative stability of surface structures with different compositions depends on the concentration of sulfur containing species in the gas phase with which the surface is in equilibrium. For the assumption of an equilibrium with H_2SO_4/H_2O and SO_3/H_2O, the pyrosulfate phase $[S_2O_7^{2-},2H^+,H_2O]$ and the proton free $[SO_3]$ phase (the tetragonal equivalent of SO_3 on the c-ZrO_2 (111) thin film), respectively, are the prevailing surface structures for wide temperature and partial pressure ranges (Fig. 10). The prevailing structure for the H_2SO_4/H_2O sulfation of the t-ZrO_2(101) surface is the pyrosulfate accompanied by one water molecule $[S_2O_7^{2+},2H^+,H_2O]$ (Fig. 11). Only for loadings of two sulfate groups per 1x2 t-ZrO_2(101) surface cell (4.3 S-atoms/nm^2), S=O vibrations above 1400 cm^{-1} are predicted by theory and pyrosulfate species have S=O vibrations in the region of 1420 – 1400 cm^{-1}.[40] Only one other different structure with ν(S=O) at about 1400 cm^{-1} was found. This is pure SO_3 adsorption, which is only possible at very high temperatures in the case of H_2SO_4 as sulfation agent or, as in the case of the single crystalline films, with SO_3 as sulfur source.

Bands at about 1400 cm^{-1} were experimentally observed for activated SZ powders.[76,109] In fact, the catalytic performance was found to be strongly dependent on the presence of this band and hence of the pyrosulfate structure.

For example, water washing of sz-mel removed approximately 40% of the initial sulfur content (Table 1) and the band at 1400 cm^{-1} for the S=O stretching vibration disapperaed.[62] Concomitantly, the catalytic activity was suppressed. However, sulfation with SO_3 resulted in recovery of the catalytic activity. Moreover, the activity increased by a factor of approximately 10 with respect to the parent sz-mel sample and the characteristic S=O band of pyrosulfate at 1400 cm^{-1} was not only restored but also increased in intensity after sulfation with gaseous SO_3. From these observations it appears that through washing, the pyrosulfate is hydrolyzed with one monosulfate unit remaining on the surface and one being dissolved. Further evidence for this scenario comes from DFT calculations which showed the sulfur atoms in the pyrosulfate to be non-equivalent (Fig. 11).

Moreover, the difference in activity between cat1 and cat2 can also be explained by the presence and absence of pyrosulfates. Only for the active cat1 bands above 1400 cm^{-1} appeared in DRIFT spectra.[92] A high sulfur density might be advantageous for the formation of condensed sulfate species such as pyrosulfate, because cat2 with the same sulfur content but a significantly higher surface area did not feature pyrosulfates at all. Consistently, DFT calculations yield pyrosulfate structures only at high coverages.[40]

The sulfation experiments on powders showed that using either ammonium sulfate or SO_3, pyrosulfate groups can be generated, and that these surface species seem to be a prerequisite for a material active for *n*-butane isomerization.

DFT calculations further showed that co-adsorption of water onto the prevailing $[S_2O_7^{2-},2H^+,H_2O]$ species ($\nu_{S=O}$ = 1421 cm^{-1}), yielding $[S_2O_7^{2-},2H^+,2H_2O]$ ($\nu_{S=O}$ = 1409 cm^{-1}), shifts the S=O band 12 cm^{-1} to lower wave numbers.[40] Such shift was indeed reported by Klose et al.[76] According to the calculated phase diagram a water rich environment causes splitting of the S—O—S bridge and loss of SO_3 which is accompanied by a shift of the former ν(S=O) down to 1260 cm^{-1}.

The distinct influence of water onto the prevailing sulfate structure may the contradicting conclusions reached in different studies on sulfated zirconia. As the preparation of sulfated zirconia is connected to precipitation in aqueous solution, activation under various atmospheres or temperatures, and variable storage conditions, the influence of water onto the formation of the surface sulfates is evident. Thus, the discussion of experimental catalytic activities should be always accompanied by a proper description of all details in the preparation process.

3.4. Acidic properties and role of Brønsted sites for the activation of n-butane

Sulfated zirconia catalysts were initially believed to be superacidic due to their ability to isomerize *n*-butane even at RT and acidity measurements using Hammett indicators.[3,83] There are, however, a number of drawbacks regarding the indicator technique, including the assumptions that an equilibrium is achieved and the active site is an isolated acid, and the ability to detect an end point. The catalytic activity of SZ has also been correlated with its acidity, although there are no consistent trends across the literature and the techniques used to evaluate the acidity often suffer from experimental problems such as reaction with SZ during temperature programmed methods rather than desorption. More recent investigations have revealed the acidity of SZ not to be stronger than that of sulfuric acid using NMR[77], UV-vis[78], IR spectroscopy,[79] and theoretical calculations.[80] Investigations into the type of sites have been made using numerous probes including pyridine and CO, although again no consistent theories have emerged to link the catalytic activity of SZ to either its Brønsted or Lewis acidic sites.[83] The characterization of an acid-base catalyst system is still a challenge as the determination of acid sites depends on the choice of appropriate probe molecules. Therefore, several techniques were employed to characterize the acidic strengths of the model systems, either by interaction with ammonia or by selective poisoning of acid surface centers in the case of powders. The main aim was to identify surface centers that are responsible for the activation of the alkane.

3.4.1. Acidic properties of supported nanocrystalline films

The acidic properties of the nanocrystalline thin films have been investigated employing ammonia as a probe molecule and both XPS and TDS as analytical techniques. XP spectra of the N 1s signal after exposure to 10000 L of ammonia, at RT, show two peaks at 402.1 eV and 400.0 eV.[33] Heating to 473 K results in a significant decrease of the higher binding energy peak while the lower binding energy species remain relatively unaffected, indicating a weakly and a strongly bound adsorbate species.

Ammonia TDS was performed on samples mounted and heated as described in ref.81. TDS profiles after activation at 723 K, under vacuum, followed by exposure to 49 hPa ammonia for 30 minutes at RT, see Fig. 12, show a broad peak from 373 to 423 K and a sharp peak centered at ca. 637 K. The ammonia desorption profile obtained for the nanocrystalline films is significantly different from the powder samples reported in this publication; however, it is similar to those of previously reported active SZ powder catalysts.[82] Sulfate fragments are detected concomitant with the high temperature peak, such fragments are seen from the non-exposed film only at temperatures above 723 K. This is consistent with earlier reports of sulfated oxides

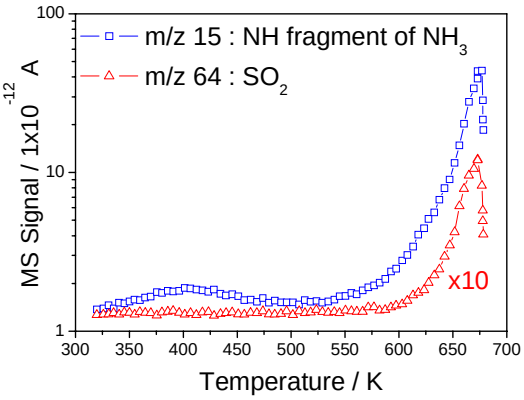

Figure 12: TDS of a 24 h deposited air-treated nanocrystalline film after exposure to 49 hPa ammonia for 30 minutes at room temperature. 750 µm thick Si substrate used with the thermocouple placed under clip on film surface.

(including SZ) more readily undergoing decomposition upon exposure to basic probe molecules at elevated temperatures.[83]

The ammonia adsorption experiments conducted on the nanocrystalline films detect two distinctly different types of sites. The stronger binding site has been shown to react at high temperatures rather than release the basic probe, which is consistent with the literature,[83] thus the acidic properties of the nanocrystalline thin films are comparable to those of active powder SZ catalysts.

3.4.2. Role of Brønsted sites for the activity of sulfated zirconia

It has been claimed that both Brønsted and Lewis acid sites are necessary for good performance of SZ catalysts.[84] The site distribution on powder samples was therefore analyzed by pyridine adsorption (see Table 1). Water washing quantitatively converted Brønsted acid sites into Lewis acid sites. This trend is consistent with earlier observations that, vice versa, upon sulfation the number of Lewis acid sites decreased while their strength increased.[85] The data in Table 1 imply a correlation of the catalytic activity with the number of Brønsted sites rather than with the number of Lewis sites.

Hence, selective poisoning of Brønsted sites was performed by using an increasing amount of sodium in form of sodium sulfate as second sulfation agent.[86] To stay comparable with cat1 and cat2, the overall sulfate content of the poisoned samples was maintained constant by just changing the ratio between the two sulfation agents ammonium and sodium sulfate in a stepwise fashion. The nominal sulfate content was exactly the same as for cat1 to enable the formation of active pyrosulfates on the surface. Samples were prepared with 3% (sample Na1) and 40% (sample Na2) poisoned centers, respectively. These samples were characterized by N_2-adsorption, XRD, XPS, and TAP as

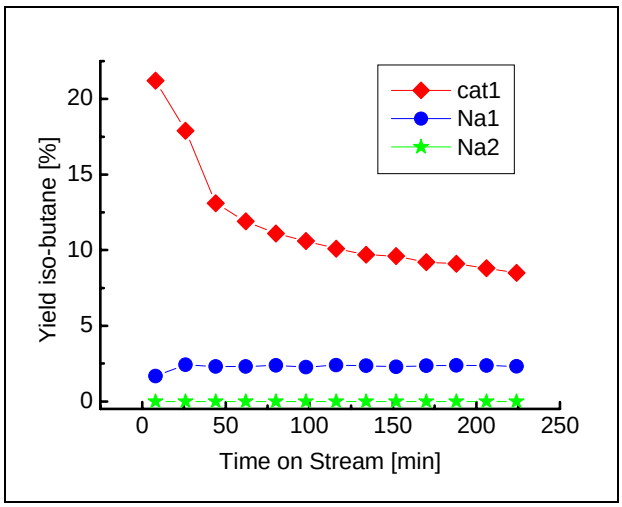

Figure 13: Comparison of catalytic activities (*n*-butane isomerization) of powder model systems unmodified (cat1) and modified by selective poisoning of Brønsted sites (Na1, Na2)

described in ref. 86. The catalytic activities of cat1 and these modified samples are compared in Fig. 13.

Catalyst cat1 displayed a high initial isomerization rate followed by a slow decrease in activity and a constant final activity of around 10 % conversion. All sodium modified samples showed a dramatically lower or no isomerization activity. Sample Na1 had a moderate activity with a yield of 3% of *iso*-butane; the sample Na2 was completely inactive. Assuming that the protons of the Brønsted acid sites were exchanged by sodium cations and that the strongest sites were exchanged first, the decreased isomerization activity for Na1 indicates that only a very small number of these most acidic Brønsted sites are involved in *n*-butane activation. Only 3% of Brønsted centers close to sulfate groups were selectively poisoned, which resulted in a significant decrease of isomerization activity. Adsorption of pyridine[86] on these samples also revealed a loss of Brønsted sites with increasing sodium amount, which supports the selective exchange of acid sites on the surface. Additional inspection by ammonia TPD showed that this method was not sensitive enough to discriminate between cat1 and Na1. As only 3 % of centers, which reflects the minority of surface centers, were poisoned, the detection limit of TPD was reached. Only for Na2 TPD was able to detect a changed profile indicating a total loss of acid centers in the high temperature zone above 600 K (see ref. 86). Poisoning of the surface Brønsted sites also influenced the appearance of the sulfates, which was elucidated by DRIFTS.[74] With increasing sodium amount, the typical S=O band for cat1 at 1402 cm^{-1} shifted to lower wave numbers indicating the loss of pyrosulfates on the surface. Additionally, transient TAP experiments were performed for the unmodified and modified powder samples to study the adsorptive interaction of *n*-butane with the surface in more detail. Fig. 14a-c shows the normalized pulse responses for cat1, Na1, and Na2. From the response curves for cat1 (Fig. 14a, time scale 5s), a strong adsorption of *n*-butane on the surface could be concluded. An extremely long desorption phase for the reactant was observed for low temperatures.[87] In contrast to this, all sodium exchanged samples showed a decreased interaction of the reactant with the surface indicated by much shorter desorption times for all temperatures (see Fig. 14b-c, time scale 1s). The average residence times

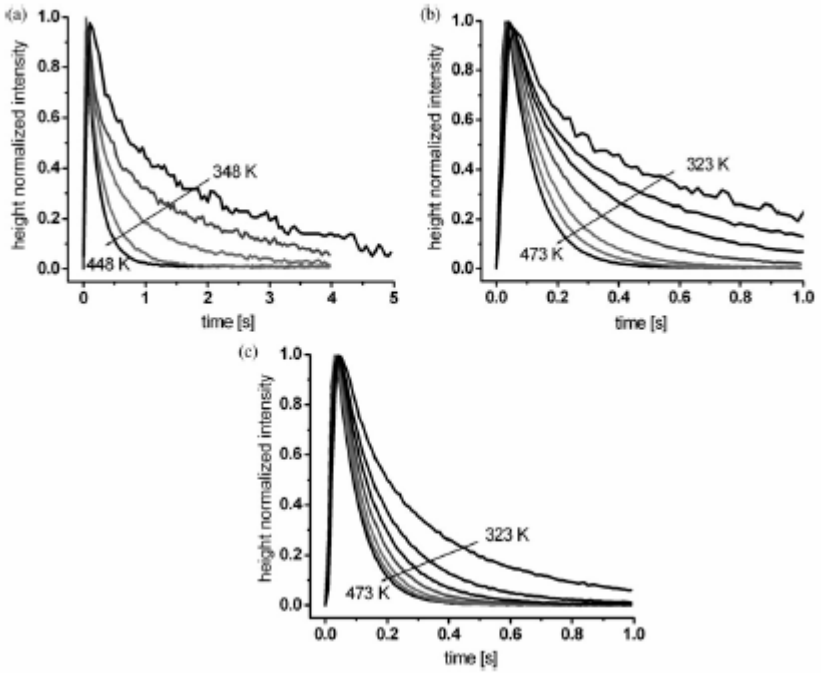

Figure 14: Pulse responses (*n*-butane) for Na-unmodified and Na-modified sulfated zirconias for different temperatures

Table 4: Deprotonation energies (DPE) of different SZ structures in kJ/mol

Structure	DPE	Most acidic proton
$[SO_3, OH^-, H^+]$	1414	$O_{b,3}$–H
$[SO_3, OH^-, H^+]$/t-ZrO_2(001)	1486	Ref. 49
$[SO_3, OH^-, H^+, H_2O]$	1499	Water O_t–H
$[SO_4^{2-}, 2H^+]$	1435	$O_{b,2+1}$–H
$[SO_4^{2-}, 2H^+]$/t-ZrO_2(001)	1354	Ref. 49
$[SO_4^{2-}, 2H^+, 3H_2O]^a$	1387	Water O_t–H
$[S_2O_7^{2-}, 2H^+, H_2O]^a$	1419	$O_{b,3}$–H
$[SO_4^{2-}, HSO_4^-, 3H^+, 2H_2O]^a$	1353	$O_{b,3}$–H
H_2SO_4	1327	Gas phase
H_3O^+	722[b]	Gas phase
Proton-exchanged Zeolite	~1200	ref. 89 and 90

[a] Most stable for certain temperature and pressure regions. The structures are described in ref. 40. (compare Fig. 8). [b] PBE/cc-pVQZ value, PW91/cc-pVQZ is 723 kJ mol^{-1}. O_t–H: terminal Zr–OH $O_{b,2+1}$–H: bridging O with a very long third Zr–O bond (>2.5 Å) $O_{b,3}$–H: bridging O with three Zr–O bonds within 2.5 Å.

of *n*-butane over the catalyst bed decreased in the TAP experiment at 423 K from 0.49 to 0.16 s for cat1 and Na1, and at 348 K from 1.58 to 0.47 s, respectively. This means the interaction of the reactant *n*-butane was shortened by the poisoning of only 3% of active surface centers by one third.

Deprotonation energies (DPE) have been calculated by DFT considering the reaction SZ-OH → SZ-O^- + H^+.[88] Table 4 shows the results obtained for various possible structures of SZ. The structures range from a single SO_3 and H_2O coadsorption ($[SO_3,OH^-,H^+]$ and $[SO_4^{2-},2H^+]$) to 2 SO_3 and 4 H_2O ($[SO_4^{2-},HSO_4^-,3H^+,2H_2O]$) per surface unit cell. For reference, pure water adsorption is listed, too. The range of the DPE of these structures is from 1370 to 1499 kJ/mol. For comparison, the gas phase H_2SO_4 has a DPE of 1327 kJ/mol, proton exchanged zeolites have a DPE of about 1200 kJ/mol.[89,90] For none of the investigated structures, an acidity higher than that of gas phase H_2SO_4 could be observed, consistent with experimental results.[77,78,79] This confirms the previous conclusion that the term 'super-acid', which was often used for SZ catalytic materials,[3] is inappropriate.

3.5. Adsorption of n-butane and other alkanes

3.5.1.Nanocrystalline thin films

The interaction of the nanocrystalline thin films with the reactant, *n*-butane, has been studied using He II (hν = 40.81 eV) UPS. Spectra were measured in adsorption-desorption equilibrium under constant gas pressures at low temperatures (RT to 100 K). Isosteric heats of adsorption can be derived from multiple isobars at different pressures and, in principle, reaction orders and frequency factors can be deduced from a fit of the isobars.[91] To study only the adsorption of *n*-butane, low pressures and temperatures were used as SZ is known to be catalytically active even at RT.[3] The sample was mounted and temperature controlled (liquid N_2 cooling and resistive heating) in a similar setup as to the one described in ref. 81. Samples were activated at 573 K in synthetic air at atmospheric pressure. UP spectra

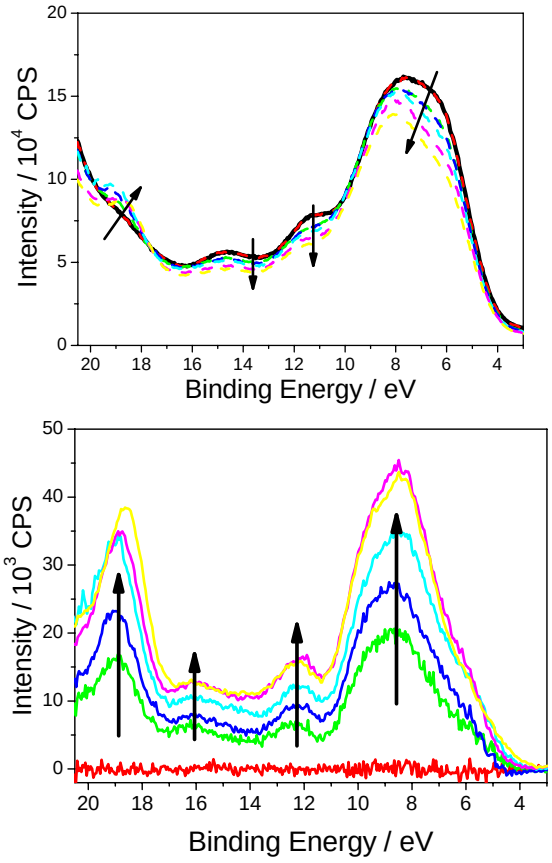

Figure 15: (a) UP Spectra of a 24 h deposited air-treated nanocrystalline thin film, on a 1.3 mm thick Si substrate, bold line: introduced in UHV, 308 K, thin dashed lines: 1x10^{-7} hPa *n*-butane, (b) corresponding difference spectra. Arrows indicate decreasing temperature from 308 K to 150 K.

of the activated sample under vacuum and in 1x10^{-7} hPa *n*-butane are shown in Fig. 15a. As the temperature is decreased all signals shift to higher binding energies due to an increase in charging. In the presence of an adsorbate, shifts are also possible as a result of changes in the work function.[91] Upon cooling, the shape of the spectra changed indicating adsorption of *n*-butane. The difference spectra (Fig. 15b) have been analyzed as outlined in ref. 91; the secondary electron curves and He II satellites have not been accounted for. The resulting adsorbate spectra resembled that of gaseous *n*-butane[91] but the features were significantly broadened. The spectra suggest a low level of perturbation and hence a weak interaction. The investigation of SZ and of its interaction with *n*-butane by UPS is only possible due to the conducting nature of the nanocrystalline thin films.

3.5.2. Sulfated zirconia powders

The differential heats of adsorption of *n*-butane (the reactant), *iso*-butane (the product), and propane (a non-reactive probe moelcule) on the SZ powders cat1 and cat2 were determined using microcalorimetry.[72] Adsorption

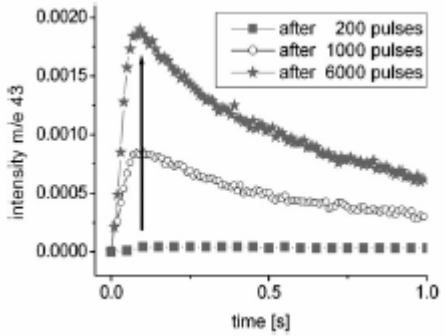

Figure 16: TAP multipulse experiment with *n*-butane on cat1.

isotherms of the materials could be adequately described using a first order Langmuir model for low pressures but a better fit at higher pressures was found with a Freundlich model (due to the slightly decreasing differential heats with coverage). Estimations of the number of sites at a typical alkane reaction pressure of 5 kPa, using the Freundlich isotherms, yielded C_4 coverages between 85 and 160 µmol g^{-1}. The disparity between the catalysts was not larger than differences arising from variations in activation temperatures. Differential heats of adsorption of approximately 50 kJ mol^{-1} were determined for all three alkane probe molecules at coverages of ca. 5 µmol g^{-1}. The heats declined to about 45 kJ mol^{-1} at a coverage of 30 µmol g^{-1}. At coverages <5 µmol g^{-1}, considerable variations in the differential heats of adsorption were observed, possibly indicating reaction on a minority of sites. However, the interaction of the alkanes with the majority of sites on the different catalysts is very weak, consistent with the *n*-butane isobar measurements on the nanocrystalline films.

The findings of the microcalorimetry investigations coincide perfectly with measurements by the transient TAP pulse method, which enables during the pulsing procedure pressure conditions slightly lower than possible with microcalorimetry. By repeated pulsing of 10^{14} molecules, a description of the "lifetime" of the catalyst from the very beginning, characterized by no coverage at all to the coverage reflected by microcalorimetry can be obtained. Moreover, it was possible to study the adsorption behavior of the reactant *n*-butane in more detail than it is feasible with calorimetry.

TAP revealed that at the beginning of all pulse experiments a small portion of *n*-butane was irreversibly adsorbed on the surface.[74,92] This effect was even more pronounced for plain zirconia,[92] and has not been described so far for SZ materials. Repeated pulsing of *n*-butane at 323 K showed that after approximately 6000 pulses a constant pulse response intensity could be observed, which was in the range of the intensity signal of non-adsorbing reactor fillings like corundum (see Fig. 16). The amount of pulsed *n*-butane was estimated as 50 µmol *n*-butane/$g_{catalyst}$, an amount which perfectly fitted to the results from microcalorimetry on these systems.[93] Moreover, assuming that one *n*-butane would hit just one sulfate/pyrosulfate, only 6% of all sulfates would have come into contact with the pulsed *n*-butane. Thus, only a limited number of surface sites is concluded to be responsible for the initial interaction of *n*-butane with the surface of sulfated zirconia agreeing perfectly with the microcalorimetry results. Modeling of the pulse responses additionally gave the opportunity to estimate heats of adsorption, which confirmed the findings of calorimetry.[94]

3.6. Reactive conversion of n-butane

3.6.1. Initiation – alkane activation

One of the central question in the mechanism of alkane activation and transformation over anion modified oxides is related to the nature of formation of the reactive intermediate, which is believed to be a carbocation-like surface species.[95] In this respect, four main pathways have been suggested. The first one is the protolytic activation of a C-H bond by formation of an alkanium ion with pentacoordinated C atom (i.e., carbonium ion), which loses H_2 to give the corresponding carbenium ion.[96] This mechanism, which has been taken from the chemistry in liquid superacids, has been criticized because theoretical and experimental studies demonstrated that sulfated zirconia materials not act as superacids.[97,98] Second, Tabora and Davis proposed that alkene impurities present in the hydrocarbon feed could yield carbenium ions by protonation on Brønsted acid sites.[99] However, the observation of catalytic activity also for alkene free feed suggests a third pathway, namely the *in situ* generation of alkenes by one electron oxidation by sulfate groups.[100] Forth, the activation of alkane was suggested to occur via hydride abstraction from Lewis acid sites.[101,102]

The reactive interaction of *n*-butane with all types of samples was investigated to elucidate the initiation of the reaction cycle and to prove the chemical reactivity of the models.

Fig. 17 shows LEED and AES results obtained for a single-crystalline film sample displaying the (√3x√3)R30° sulfation structure that was exposed at RT to *n*-butane (pressure $2x10^{-8}$ hPa). During exposure, a strong background developed in LEED and a growing C signal was measured with AES, not only during RT exposure but also after UHV annealing at 400 K (Fig. 17). Obviously, during *n*-butane interaction a C containing layer has been formed. This layer grows in an amorphous structure and induces the strong background in LEED. Isobaric measurements on the nanocrystalline films proved that physisorption of *n*-butane does not occur under these conditions (see section 3.5.1). Hence, *n*-butane molecules must have reacted with the sulfated ZrO_2 film to form stable surface species. The growing C signal measured in AES can be used as a signature of the chemical activity of the (√3x√3)R30° sulfation structure. However, the formed C-containing surface species does not destroy the (√3x√3)R30° sulfation structure. The latter was still visible even after 60 L exposure despite the large background. As a result of the reaction, the Zr and

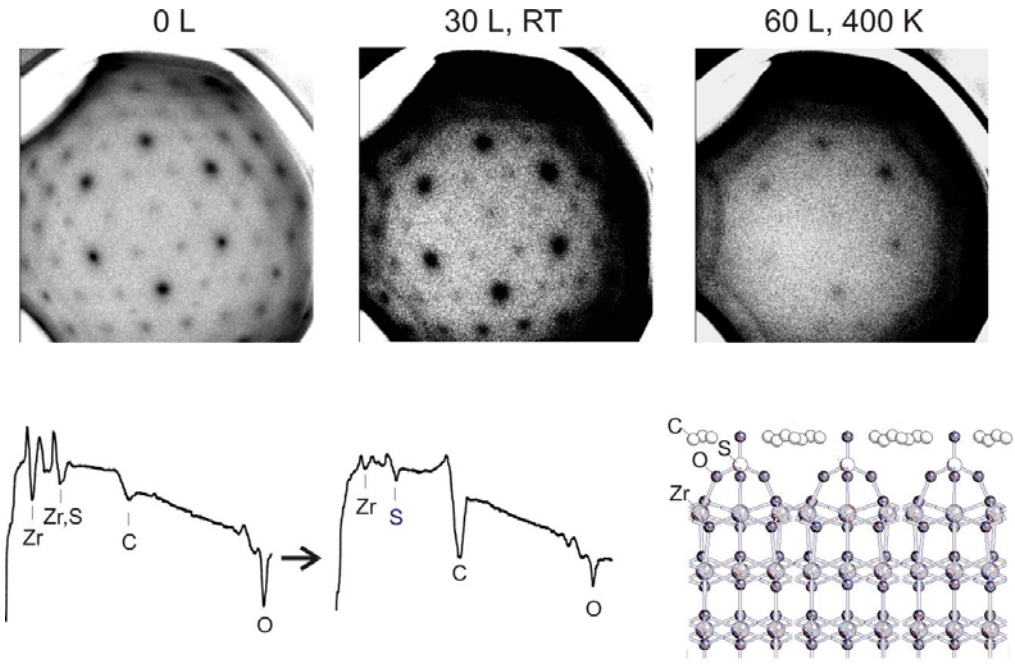

Figure 17: Interaction of *n*-butane with a sulfated ZrO_2(111) thin film sample (thickness 10 ML) studied by means of LEED and AES. During n-butan exposure, a strong background develops in LEED without destroying the pattern of the (√3x√3)R30° sulfation structure. The *n*-butane exposure started 12 h after sample sulfation which explains the slight C contamination initially measured in AES. During *n*-butane exposure, a strong C peak developed indicating chemical reactivity of the (√3x√3)R30° sulfation structure and the formation of an amorphous coke-like layer. As that layer attenuates the Zr AES signals much stronger than the S signal one can conclude that the coke accumulates rather between the SO_3 complexes of the sulfation structure instead on top of them as indicated by the hard sphere model.

S signal intensities at 92 and 152 eV are reduced. However, the Zr signal is attenuated much stronger than the S signal during the *n*-butane exposure. Using the O signal for normalization, one actually finds that the attenuation factor of the Zr Auger electron intensity is three times larger than that of the S Auger electrons. Since the energies and hence the escape depths of the considered Zr and S Auger electrons are comparable, this observation rules out a carbon species in form of a continuous layer above the sulfated surface. Instead, one has to assume that the carbon species rather aggregate between the SO_3 complexes of the (√3x√3)R30° sulfation structure than on top of them. A corresponding model of the amorphous C containing surface species is visualized in Fig. 17. The observed species could either be an intermediate or a side product.

Reaction of the nanocrystalline SZ thin films with *n*-butane was studied using *in-situ* XPS and NEXAFS. Experiments were performed using the undulator beam line U49-2/PGM2 at the BESSY synchrotron facility; details of the setup are described in ref.103. C1s XP spectra were recorded using a photon energy of 470 eV. Binding energies were corrected using Zr $3d_{5/2}$ = 182.2 eV of ZrO_2.[68] The Auger C K edge NEXAFS spectra were calibrated by aligning the C1s π* (C=C) transition of graphite to 285.38 eV.[104] Beam-induced carbon deposition was observed during measurements in presence of *n*-butane in the gas phase. C1s XP spectra were then acquired in UHV from areas that were not irradiated during *n*-butane exposure, after consecutive treatments of 0.5 hPa *n*-butane at 548 K and 200 hPa *n*-butane at maximally 481 K. Stable carbon-containing surface species were detected, similar to the findings made with the single-crystalline films. The formation of such species indicates that the nanocrystalline thin films contain reactive centers (Fig. 18). The observed species contain carbon in at least two different environments, as shown in Fig. 18a (spectrum of the activated surface subtracted). The main peak at 284.2 eV corresponds to hydrocarbon species and the minor component at 288.8 eV relates to oxygenated carbon species; the former component increases with the subsequent *n*-butane exposures whereas the latter does not change significantly. The formation of such carbon surface species on the surface proves that the nanocrystalline thin films contain reactive centers.

Auger electron yield NEXAFS analysis of the C K edge after the fore-mentioned *n*-butane subsequent exposures (Fig. 18b), analyzed as outlined in ref.105, shows the development of a feature at ~285.1 eV. This transition is not consistent with absorbance features arising from the reactant, *n*-butane, or the isomerization product, *iso*-butane.[106] The observed transition is however characteristic of π* resonances from unsaturated sp or sp^2 carbon bonds and is consistent with unsaturated hydrocarbon species such as butenes[107] and also amorphous carbon.[108] The unsaturated species is speculated to result from the initiation step of the oxidative dehydrogenation, possibly a side product from this initiation step.

All catalytic experiments and theoretical findings[109] point towards a mechanism involving activation of *n*-butane at low temperatures through oxidative dehydrogena

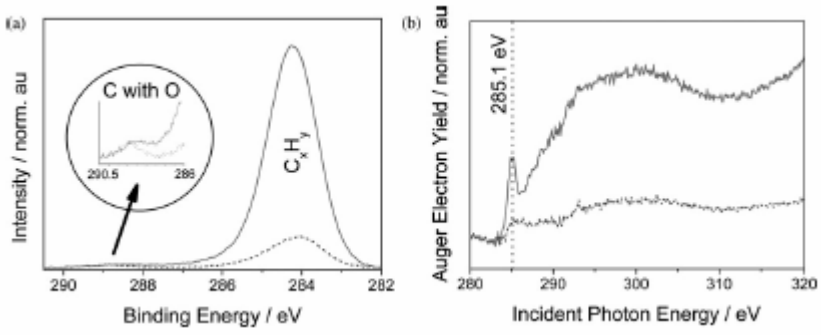

Figure 18: C 1s XP Spectra (a) and NEXAFS (b) of an air-treated nanocrystalline thin film, on a 1.3 mm thick Si substrate, in UHV after subsequent treatments of 0.5 hPa *n*-butane at 578 K for 80 minutes (dashed line) and 200 hPa *n*-butane ramped from 323 K to 481 K at 10 K/min (solid line).

tion to butene (eqn. (1)) by labile (water soluble) sulfate groups:

$$C_4H_{10} + SO_3 \rightarrow C_4H_8 + SO_2 + H_2O \qquad (1)$$

For the first time, all three products involved in this activation step could be identified.[109] For this purpose, three different analytical techniques were successfully combined. Temperature-programmed desorption/reaction of *n*-butane on sulfated zirconia showed that butene can be formed at 373 K. Water and SO_2, the other two expected products from oxidative dehydrogenation of *n*-butane, were not detected during butene desorption due to their stronger adsorption on sulfated oxides. However, water was identified by *in situ* IR spectroscopy from the increase of the intensity of the bending vibration at 1600 cm^{-1}. A linear correlation between the intensity of this band and the reaction rate during the induction period clearly indicated that the rate determining step is the oxidative dehydrogenation of *n*-butane.[76] On the other side, under steady-state conditions, when the surface concentration of carbenium ions obtained by protonation of *n*-butane molecules remains constant, the rate of increase of this band was strongly reduced. Finally, SO_2 was identified and quantified by ion chromatographic analysis of the solution obtained by trapping the effluent in NaOH solution of the reactor while increasing the reactor temperature under inert flow.

The favorable reaction energies for the oxidative dehydrogenation of *n*-butane according to eqn. (2) explain the initial butene formation:

$$C_4H_{10} + 1\times 2\,\text{t-}ZrO_2(101)\cdot nSO_3\cdot mH_2O \rightarrow C_4H_8 + 1\times 2\,\text{t-}ZrO_2(101)\cdot(n-1)SO_3\cdot SO_2 \cdot(m+1)H_2O \qquad (2)$$

Table 5 shows the calculated energies for this reaction. For surface structures with a single sulfur atom per t-ZrO_2(101) (1x2) surface unit cell, the reaction energies are positive (6 to 47 kJ/mol depending on the water content), while structures with two sulfur atoms per cell have negative reaction energies (-10 to –67 kJ/mol). The reaction of one of the dominating pyrosulfate surface structures, [$S_2O_7^{2-}$,$2H^+$,H_2O], with *n*-butane yields [SO_4^{2-},SO_2,$2H^+$,$2H_2O$] on the surface (reaction energy -10 kJ/mol). The structure contains adsorbed SO_2 as found in the experiments, too. In this reaction, the pyrosulfate splits into a tri-dentate sulfate species and SO_2 which is not directly coordinated to the surface but *via* two hydrogen bonds only to two water molecules. The energy expense for the removal of SO_2 is 34 kJ/mol. The less stable pyrosulfite structure would look like shown in Fig. 11, with one oxygen atom removed. Reaction (see eqn. (2)) does not consider adsorption of *n*-butane/butene on the SZ surface. In the gas phase, the oxidative dehydrogenation of *n*-butane by SO_3 (eqn. (2)) is also thermodynamically favored. The calculated reaction enthalpy at 298 K is –11 kJ/mol (reaction energy -14 kJ/mol) and the corresponding experimental gas phase value is -28 kJ/mol.[110] The difference of 17 kJ/mol is in the expected error range of DFT calculations.

Table 5: Calculated total reaction energy, ΔE_{total} in kJ/mol, of different SZ structures with n-butane following eqn (2).

SZ	SZ_{red}, OH_2	ΔE_{total}
[SO_3][a]	[SO_2, OH^-, H^+]	37.1
[SO_3, OH^-, H^+]	[SO_2, OH^-, H^+, H_2O]	47.0
[SO_4^{2-}, $2H^+$]	[SO_3^{2-},$2H^+$, OH^-,H^+]	5.6
[$2SO_3$][a]	[SO_4^{2-}, SO_2, $2H^+$]	–36.1
[$S_2O_7^{2-}$, $2H^+$]	[$S_2O_6^{2-}$, $2H^+$, H_2O]	–66.8
[$S_2O_7^{2-}$, $2H^+$, H_2O][a]	[SO_4^{2-}, SO_2, $2H^+$, $2H_2O$]	–10.1
[SO_4^{2-}, HSO_4^-, $3H^+$][a]	[$S_2O_6^{2-}$, $2H^+$, $2H_2O$]	–26.7
H_2SO_4 (gas)	SO_2 + $2H_2O$	68.2
SO_3 (gas)	SO_2 + H_2O	–13.8

[a] These structures are most stable for specific pressure and temperature regions.

Furthermore, confirmation of *n*-butane activation via oxidative dehydrogenation on sulfated zirconia was provided by catalytic experiments with H_2 or O_2 added to the feed.[109] H_2 decreased the catalytic activity, which can be explained by a lowering of the alkene concentration, while O_2 led to an increase in activity by furthering the initiation oxidative dehydrogenation but also to more rapid deactivation.

Theory and experiment show that pyrosulfates are the prevailing species after a typical activation and can react with *n*-butane in an oxidative dehydrogenation to yield butene. On the other hand, TAP and calorimetry evidence a weak interaction of butane with the majority of sites and Na poisoning experiments demonstrate that the

number of sites actually active for butane isomerization is small. Apparently, not all pyrsosulfates react at least not immediately as the slow induction of the reaction indicates.[76] Limiting could also be the further conversion to carbenium ions by protonation, either because of the small number of sites capable of protonation or because of blocking of Brønsted sites by equilibrium adsorption of butane.[111] The detrimental effect of a small amount of Na^+ speaks for the importance of a minority of sites, which must originate from irregularities in the zirconia surface. Evidence already exists for the presence of defects in zirconia, from preparative studies[21] and from investigations on promoted materials, which show that many promoter cations dissolve in the zirconia lattice[112] and will generate defects near the surface. [113]

3.6.2. Isomerization mechanism

The second aspect that is still disputed is the pathway of transformation of the carbocationic species formed in the activation step. Two main routes were suggested.[95,114,115,116,117,118,119] The intramolecular (monomolecular) mechanism involves the isomerization of a butyl cation with formation of a primary carbenium ion, which in liquid phase would be associated with a high energy barrier but on the surface could be stabilized in form of an alkoxide. Alternatively, an intermolecular (bimolecular) route with formation of a C_8 carbocation followed by isomerization and ß-scission steps was proposed.[115] Support for both mechanisms has been provided by labeling experiments with ^{13}C-labeled *n*-butane and kinetic studies analyzing the product distribution in function of the conversion.[23,120,121,122] A more involved picture was presented by Ahmad et al.[123], who proposed a predominantly monomolecular mechanism during the induction period and at long times on stream, but a bimolecular mechanism at higher conversions.

The extrapolation of the product distribution at zero conversion showed that *iso*-butane is the only kinetically primary product obtained by intramolecular isomerization, while pentane and propane are secondary (and tertiary products) formed by a consecutive intermolecular step involving alkylation and subsequent ß-cracking of the C_8 moieties formed.[124] Transient kinetic experiments proved that under differential conditions and at steady state, the rate determining step is the intramolecular conversion of the *sec*-butyl cation to the *tert*-butyl cation. In fact, the concentration of the first species was found to be two orders of magnitude above that of the latter. The catalytic cycle is then closed by hydride transfer to the *tert*-butyl cation ion by an *n*-butane molecule which is thus activated. Based on these results, the sequence of steps involved in *n*-butane isomerization (eqn. (3a-e)) was established as: a-b) stoichiometric activation of *n*-butane; c-d) chain propagation; e) termination.

$$n\text{-}C_4H_{10} + SO_3 \xrightarrow{k_{n1}} n\text{-}C_4H_8 + SO_2 + H_2O \qquad (3a)$$

$$n\text{-}C_4H_8 + H^+ \underset{k_{n-2}}{\overset{k_{n2}}{\rightleftharpoons}} sec\text{-}C_4H_9^+ \qquad (3b)$$

$$sec\text{-}C_4H_9^+ \underset{k_{n-3}}{\overset{k_{n3}}{\rightleftharpoons}} tert\text{-}C_4H_9^+ \qquad (3c)$$

$$tert\text{-}C_4H_9^+ + n\text{-}C_4H_{10} \underset{k_{n-4}}{\overset{k_{n4}}{\rightleftharpoons}} i\text{-}C_4H_{10} + sec\text{-}C_4H_9^+ \qquad (3d)$$

$$n\text{-}C_4H_8 + T \xrightarrow{k_{n5}} n\text{-}C_4H_8 - T \qquad (3e)$$

From the mechanistic model, the overall isomerization reaction rate r_n is proportional to the concentration of Brønsted acid sites C_B, the active sulfate species $[SO_3]$ and the partial pressure of *n*-butane p_n (see eqn. (4)). T indicates a terminating site.

$$r_n = \frac{k_{n1}k_{n2}k_{n3}C_B[SO_3]p_n}{[T]k_{n5}(k_{n-2}+k_{n3}) + k_{n1}k_{n2}[SO_3]p_n} \qquad (4)$$

As illustrated in Fig. 19 an excellent agreement between the kinetic model and the experimental data obtained for both *n*- and *iso*-butane isomerization under differential conditions was obtained. The overall mechanism found by the catalytic and theoretical experiments is summarized in Fig. 20.

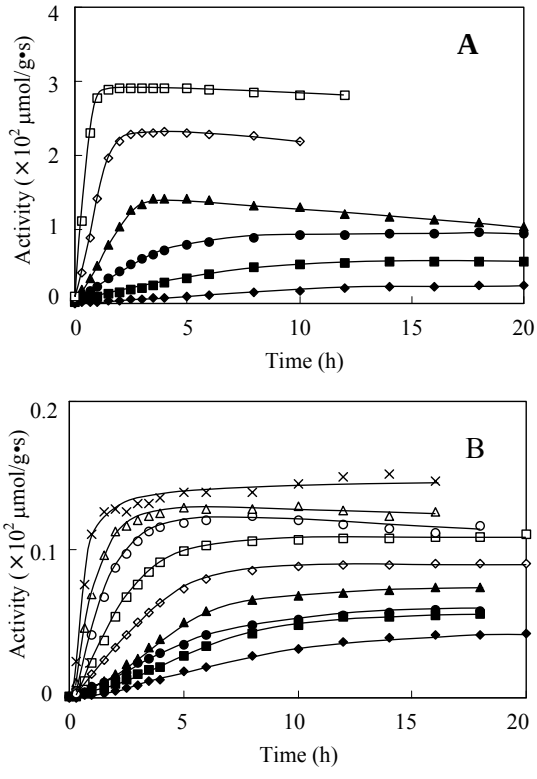

Figure 19: Fitting of the kinetic experimental data for *n*-butane (A) and *iso*-butane (B) isomerization with our kinetic model (continuous lines)

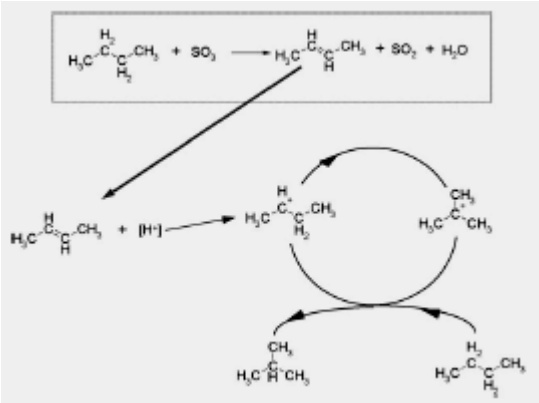

Figure 20: Overall mechanism of *n*-butane isomerization at low temperature and differential conditions on sulfated zirconia.

4. Conclusions

A surface phase diagram of zirconia in interaction with SO_3 and water was established by DFT calculations. The nature of the obtained surface structures was proven through experiments in different sections of the diagram. Upon SO_3 adsorption on single-crystalline zirconia films in a water-free environment, a ($\sqrt{3}$x$\sqrt{3}$)R30° sulfation structure which is stable up to 650 K is experimentally identified. DFT calculations show that in the given pressure and temperature range the ($\sqrt{3}$x$\sqrt{3}$)R30° structure is the equilibrium one with a C_3 symmetry and three equivalent S-O-Zr bonds. IR spectroscopy on powders with different sulfur content showed the formation of a condensed species at high surface concentrations, i.e., a pyrosulfate species. With increasing surface water concentration, the characteristic high frequency (≈1400 cm^{-1}) S=O vibration of this species is shifted to lower wavenumbers in agreement with theory. In aqueous medium, the S-O-S bridge is hydrolyzed and the pyrosulfate is partially dissolved. The congruence between theory and experimental data indicates that equilibrium structures are observed in the experiments.

The catalytic activity of sulfated zirconia powders in *n*-butane isomerization was found to be related to the presence of pyrosulfate species for a number of samples with variation in sulfate content and preparation. Indeed, theoretical calculations showed that it is feasible to activate *n*-butane in an oxidative dehydrogenation step to give butene, water, and SO_2. All three products are detected applying temperature programmed desorption, IR spectroscopy and ion chromatography to powder samples, confirming the theory. Carbon-containing species were also detected on the surface of single- and nanocrystalline sulfated thin films after exposure to *n*-butane, on the nanocrystalline films they could be identified as unsaturated ones.

The phase diagram indicates that after activation treatments, pyrosulfate is the prevailing structure on the surface. Adsorption experiments, however, showed that the interaction of *n*-butane with the majority of the sites on nanocrystalline films and on powders is weak (≈50 kJ/mol) and reversible. IR spectra show that *n*-butane attaches to surface OH groups, which according to theory are Zr-OH and not S-OH groups. Although intense vibrations in the IR spectra suggest that pyrosulfate is an abundant species on the surface, conversion of *n*-butane seems to occur only on a minority of sites of less than ≈5 µmol/g. This was the range in which somewhat higher heats of interaction were observed in the calorimetric measurements, with an expected value of only about 70 kJ mol^{-1} for the ODH reaction according to theory. Consistent with the hypothesis of very few sites, it was possible to almost completely poison the catalyst by adding Na^+ ions corresponding to a minority of sulfate sites. The changes induced to the surface sites by Na^+ were outside the detection limit of typical characterization methods such as ammonia TPD. Future research will have to clarify what distinguishes these few sites. It is hypothesized that irregularities in the surface of the zirconia support - whose role is not fully understood - are responsible.

Despite the wide variety of samples used and the large range of reactant pressures employed, the results are consistent. The chemistry of alkanes on the surface of sulfated zirconia thus does not show any unusual pressure dependency. The application of surface science techniques has proven fruitful not only for structural investigations but also for adsorption studies. Identification of surface reaction intermediates for this catalyst-reactant combination is difficult, because the number of actual conversions is small and hence the concentration of such intermediates is low. Furthermore, the active sites seem to differ only slightly in nature from the majority of sites, and also the intermediates have to be identified among the much more abundant weakly adsorbed alkanes.

Acknowledgements

The authors would like to thank Hermann Sauer and Gisela Weinberg for electron microscopy, Wolfgang Ranke for help with UPS measurements and interpretation, Michael Hävecker and Elaine Vass for support at BESSY, and Robert Schlögl for continuous support of the project. Further thanks to Christina Knöfel and Silke Matysik for help with preparation of powder samples, Frau Bettina Rulle for N_2-adsorption measurements, Ralf Kulla for technical and engineering STM support. Valuable discussion and experimental input from Katsutoshi Nagaoka and Olga Manoilova are highly appreciated. We also gratefully acknowledge the center for Bundeshöchstleistungsrechnen in Bayern and the Norddeutscher Verbund für Hoch- und Höchstleistungsrechenzentrum for computer time. We thank Konrad Hayek, Innsbruck, for fruitful discussions. The project was funded by the DFG priory program (SPP) 1091 "Bridging the Pressure and Material Gap in Heterogeneous Catalysis", individual projects Pa 194/9, Le 1187/2, Je 267/1, Wi 1164/4 and Sa 582/5.

References and Notes

[1] G. D. Yadav and J. J. Nair, *Microporous Mesoporous Mater.,* 1999, **33,** 1-48.

[2] V. C. F. Holm and G. C. Bailey, *US Pat.,* 3 032 599, 1962.

[3] M. Hino, S. Kobayashi and K. Arata, *J. Am. Chem. Soc.*, 1979, **101**, 6439–6441.

[4] M. Hino and K. Arata, *J. Chem. Soc. Chem. Commun.,* 1980, 851-852.

[5] T. Jin, T. Yamaguchi and K. Tanabe, *J. Phys. Chem.,* 1986, **90,** 4794-4796.

[6] A. Clearfield, G. P. D. Serrette and A. H. Khazi-Syed, *Catal. Today,* 1994, **20,** 295-312.

[7] R. A. Keogh, R. Srinivasan and B. H. Davis, *J. Catal.,* 1995, **151**, 292-299.

[8] G. K. Chuah, S. Jänicke and B. K. Pong, *J. Catal,.* 1998, **175,** 80-92.

[9] T. Yamaguchi, *Catal. Today,* 1994, **20,** 199-218.

[10] R. C. Garvie, *J. Phys. Chem.,* 1965, **69,** 1238-1243.

[11] J. M. Parera, *Catal. Today,* 1992, **15,** 481-490.

[12] M. Bensitel, O. Saur, J. C. Lavally and G. Mabilon, *Mater. Chem. Phys.,* 1987, **17,** 249-258.

[13] V. Pârvulescu, S. Coman, P. Grange and V. I. Pârvulescu, *Appl. Catal., A,* 1999, **176,** 27-43.

[14] K. Arata, *Appl. Catal., A,* 1996, **146,** 3-32.

[15] P. A. P. Nascente, *J. Mol. Catal. A: Chem.,* 2005, **228,** 145-150.

[16] J J. A. Moreno and G. Poncelet, *Appl. Catal., A,* 2001, **210,** 151-164.

[17] T. Yamaguchi, *Appl. Catal.,* 1990, **61,** 1-25.

[18] A. Corma, *Chem. Rev.,* 1995, **95,** 559-614.

[19] R. A. Comelli, S. A. Canavese, S. R. Vaudagna and N. S. Figoli, *Appl. Catal., A,* 1996, **135,** 287-299.

[20] V. Adeeva, J. W. de Haan, J. Janchen, G. D. Lei, V. Schunemann, L. J. M. van de Ven, W. H. M. Sachtler and R. A. van Santen. *J. Catal.,* 1995, **151,** 364-372.

[21] A. H. P. Hahn, R. E. Jentoft, T. Ressler, G. Weinberg, R. Schlögl and F. C. Jentoft, *J. Catal.,* 2005, **236,** 324-334.

[22] H.-J. Freund, H. Kuhlenbeck and V. Staemmler, *Rep. Prog. Phys.,* 1996, **59,** 283-347.

[23] V. Maurice, M. Salmeron and G. A. Somorjai, *Surf. Sci.,* 1990, **237,** 116-126.

[24] I. Sebastian, T. Bertrams, K. Meinel and H. Neddermeyer, *Faraday Discuss.,* 1999, **114,** 129-140.

[25] C. Hagendorf, R. Shantyr, K. Meinel, K.-M. Schindler and H. Neddermeyer, Surf. Sci., 2003**, 532-535,** 346-350.

[26] R. Shantyr, C. Hagendorf and H. Neddermeyer, *Surf. Sci.,* 2004, **566-568,** 68-73.

[27] C. Hagendorf, R. Shantyr, H. Neddermeyer and W. Widdra, *Phys. Chem. Chem. Phys.,* 2006, **8,** 1575-1583.

[28] K. Meinel, K.-M. Schindler and H. Neddermeyer, *Surf. Sci.,* 2003, **532-535,** 420-424.

[29] K. Meinel, A. Eichler, K.-M. Schindler and H. Neddermeyer, *Surf. Sci.,* 2004, **562,** 204-218.

[30] M. Hohage, T. Michely and G. Comsa, *Surf. Sci.,* 1995, **337,** 249-267.

[31] K. Meinel, A. Hofmann, S. Förster, R. Kulla, K.-M. Schindler, H. Neddermeyer, J. Sauer and W. Widdra, *Phys. Chem. Chem. Phys.,* 2006, **8,** 1593-1600.

[32] M. Agarwal, M. R. De Guire and A. H. Heuer, *J. Am. Ceram. Soc.,* 1997, **80,** 2967-2981.

[33] F. C. Jentoft, A. Fischer, G. Weinberg, U. Wild and R. Schlögl, *Stud. Surf. Sci. Catal.,* 2000, **130,** 209-214.

[34] A. D. Polli, T. Wagner, A. Fischer, G. Weinberg, F. C. Jentoft, R. Schlögl and M. Rühle, *Thin Solid Films,* 2000, **379,** 122-127.

[35] H. Cölfen, H. Schnablegger, A. Fischer, F. C. Jentoft, G. Weinberg and R. Schlögl, *Langmuir,* 2002, **18,** 3500-3509.

[36] V. V. Roddatis, D. S. Su, F. C. Jentoft and R. Schlögl, *Philos. Mag. A.,* 2002, **82,** 2825-2839.

[37] C. Albrecht, Dissertation thesis 1999 University Leipzig.

[38] X. Li, K. Nagaoka, R. Olindo and J. A. Lercher, *J. Catal.,* 2006, **238,** 39-45.

[39] htttp://cms.mpi.univie.ac.at/vasp/

[40] A. Hofmann and J. Sauer, *J. Phys. Chem. B,* 2004, **108,** 14652-14662.

[41] J. D. McCullough and K. N. Trueblood, *Acta Crystallogr.,* 1959, **12,** 507-511.

[42] G. Teufer, *Acta Crystallogr.,* 1962, **15,** 1187.

[43] D. K. Smith and C. F. Cline, *J. Am. Ceram. Soc.,* 1962, **45,** 249-250.

[44] C. Morterra, G. Cerrato and S. Di Ciero, *Appl. Surf. Sci.,* 1998, **126,** 107-128.

[45] V. Bolis, G. Magnaccia, G. Cerrato and C. Morterra, *Thermochim. Acta,* 2001, **379,** 147-161.

[46] C. Li and M. Li, *J. Raman Spectrosc.,* 2002, **33,** 301-308.

[47] R. C. Garvie and M. F. Goss, *J. Mater. Sci.,* 1986, **21,** 1253-1257; R. C. Garvie, *J. Phys. Chem.,* 1965, **69,** 1238-1243; R. C. Garvie, *J. Phys. Chem.,* 1978, **82,** 218-224.

[48] A. Christensen and E. A. Carter, *Phys. Rev. B,* 1998, **58,** 8050-8064.

[49] F. Haase and J. Sauer, *J. Am. Chem. Soc.,* 1998, **120***,* 13503-13512.

[50] J. R. Lou, U. Hess and K. A. R. Mitchell, *Appl. Surf. Sci.,* 1992, **62,** 175-180.

[51] G. Ketteler, W. Ranke and R. Schlögl, *Phys. Chem. Chem. Phys.,* 2004, **6,** 205-208.

[52] A. Paulidou and R. M. Nix, *Phys. Chem. Chem. Phys.,* 2005, **7,** 1482-2489.

[53] K. Meinel, K.-M. Schindler and H. Neddermeyer, *Surf. Sci.,* 2002, **515,** 226-234.

[54] K. Meinel, M. Klaua and H. Bethge, *J. Cryst. Growth,* 1988, **89**, 447-458.

[55] K. Meinel, A. Eichler, S. Förster, K.-M. Schindler, H. Neddermeyer and W. Widdra, *Phys. Rev. B,* 2006, **74,** 235444.

[56] A. Eichler, *Phys. Rev. B,* 2003, **68,** 205408.

[57] N. Katada, J. Endo, K. Notsu, N. Yasunobu, N. Naito and M. Niwa. *J. Phys. Chem. B,* 2000, **104,** 10321-10328.

[58] C. R. Vera, C. L, Pieck, K. Shimizu and J. M. Parera, *Appl. Catal., A,* 2002, **230,** 137-151.

[59] C. Sarzanini, G. Sacchero, F. Pinna, M. Signorotto, G. Cerrato and C. Morterra, *J. Mater. Chem.,* 1995, **5,** 353-360.

[60] C. Breitkopf, A. Garsuch and H. Papp, *Appl. Catal., A,* 2005, **296,** 148-156.

[61] H. K. Mishra and K. M. Parida, *Appl. Catal., A,* 2002, **224,** 179-189; H. K. Mishra, A. K. Dalai, D. D. Das, K. M. Parida and N. C. Pradhan. *J. Colloid Interface Sci.,* 2004, **272,** 378-383; R. L. Marcus, R. D. Gonzalez, E. L. Kugler and A. Auroux, *Chem. Eng. Commun.,* 2003, **190,** 1601-1619.

[62] X. Li, K. Nagaoka and J. A. Lercher, *J. Catal.,* 2004, **227,** 130-137.

[63] K. Arata, M. Hino and N. Yamagata, *Bull. Chem. Soc. Jpn.,* 1990, **63,** 244-246.

[64] Cell volumes V of c-ZrO_2 (V=130.32 Å3, ref. **Fehler! Textmarke nicht definiert.**) and t-ZrO_2 (2*V=139.65 Å3, ref. **Fehler! Textmarke nicht definiert.**).

[65] C. Morterra, G. Cerrato, F. Pinna and M. Signoretto, *J. Catal.,* 1995, **157,** 109-123.
[66] M. Hino, S. Kobayashi and K. Arata, *J. Am. Chem. Soc.,* 1979, **101,** 6439-6441.
[67] X. Li, K. Nagaoka, L. J. Simon, R. Olindo and J. A. Lercher, *Catal. Lett.,* accepted, for publication, DOI: 10.1007/s10562-006-9005-5.
[68] J. F. Moulder, W. F. Stickle, P. E. Sobol and K. D. Bomben, *Handbook of X-Ray Photoelectron Spectroscopy*, Perkin-Elmer, Physical Electronics Division, 1992.
[69] C. D. Wagner, L. E. Davis, M. V. Zeller, J. A. Taylor, R. M. Raymond and L. H. Gale, *Surf. Interface Anal.,* 1981, **3,** 211-225.
[70] M. P. Seah and W. A. Dench, *Surf. Interface Anal.,* 1979, **1,** 2-11.
[71] C. Breitkopf and H. Papp, DGMK Tagungsbericht, Proceedings of the DGMK-Conference, *C4/C5-Hydrocarbons: Routes to Higher Value-Added Products*, 233-240, 2004.
[72] X. Li, K. Nagaoka, L. J. Simon, J. A. Lercher, S. Wrabetz, F. C. Jentoft, C. Breitkopf, S. Matysik and H. Papp, *J. Catal.,* 2005, **230,** 214-225.
[73] B. S. Klose, Dissertation, Technische Universität Berlin, 2005. http://opus.kobv.de/tuberlin/volltexte/2005/1177/
[74] C. Breitkopf, unpublished work.
[75] D. J. Zalewski, S. Alerasool and P. K. Doolin, *Catal. Today,* 1999, **53,** 419-432.
[76] B. Klose, F. C. Jentoft and R. Schlögl, J. Catal., 2005, 233, 68.
[77] J. B. Nicholas, J. F. Haw, L. W. Beck, T. R. Krawietz and D. B. Ferguson, *J. Am. Chem. Soc.,* 1995, **117,** 12350-12351.
[78] B. S. Umansky and W. K. Hall, *J. Catal.,* 1990, **124,** 97-108.
[79] L. M. Kustov, V. B. Kazansky, F. Figueras and D. Tichit, *J. Catal.,* 1994, **150,** 143-149.
[80] F. Babou, B. Bigot and P. Sautet, *J. Phys. Chem.,* 1993, **97,** 11501-11509.
[81] W. Weiss, M. Ritter, D. Zscherpel, M. Swoboda and R. Schlögl, *J. Vac. Sci. Technol., A,* 1998, **16,** 21-29.
[82] A. Corma, M. I. Juan-Rajadell, J. M. López-Nieto, A. Martinez and C. Martinez, *Appl. Catal., A,* 1994, **111,** 175-189.
[83] X. Song and A. Sayari, *Catal. Rev. Sci. Eng.,* 1996, **38,** 329-412.
[84] J. H. Lunsford, H. Sang, S. M. Campbel, C.-H. Liang and R. G. Anthony, *Catal. Lett.,* 1994, **27,** 305-314.
[85] V. Bolis, G. Magnacca, G. Cerrato, C. Morterra, *Topics in Catal.,* 2002, **19,** 259-269.
[86] C. Breitkopf, S. Matysik and H. Papp, *Appl. Catal., A,* 2006, **301,** 1-8.
[87] C. Breitkopf, *J. Mol. Catal. A: Chem.,* 2005, **226,** 269-278.
[88] A. Hofmann and J. Sauer, to be published.
[89] M. Brändle and J. Sauer, *J. Am. Chem. Soc*. 1998, **120**, 1556-1660.
[90] F. Haase and J. Sauer, *Microp. Mesop. Mater.,* 2000, **379**, 35-36.
[91] W. Ranke and Y. Joseph, *Phys. Chem. Chem. Phys.,* 2002, **4,** 2483-2498.
[92] C. Breitkopf, Habilitation thesis, University Leipzig, 2006.
[93] F. C. Jentoft, Habilitation thesis, Humboldt-University zu Berlin, 2005.
[94] C. Breitkopf and H. Papp, Proceedings of the 1st International Conference on Diffusion in Solids and Liquids, DSL-2005, Aveiro, Portugal, 2005, 67-70.
[95] J. Sommer, R. Jost and M. Hachoumy, *Catal. Today,* 1997, **38,** 309-319.
[96] T. K. Cheung and B. C. Gates, *Chem. Commun.,* 1996, 1937-1938.
[97] B. Umansky, J. Engelhardt and W. K. Hall, *J. Catal.,* 1991, **127,** 128-140.
[98] F. Babou, G. Coudurier and J. C. Vedrine, *J. Catal.,* 1995, **152,** 341-349.
[99] J. E. Tabora and R. J. Davis, *J. Am. Chem. Soc.,* 1996, **118,** 12240-12241.
[100] D. Fărcaşiu, A. Ghenciu and J. Q. Li, *J. Catal.,* 1996, **158,** 116-127.
[101] M. Marczewski, *J. Chem. Soc., Faraday Trans.,* 1986, 82, 1687-1701
[102] M. Marczewski, *Bull. Soc. Chim. Fr.,* 1986, 750-755.
[103] H. Bluhm, M. Hävecker, A. Knop-Gericke, E. Kleimenov, R. Schlögl, D. Teschner, V. I. Bukhtiyarov, D. F. Ogletree and M. Salmeron, *J. Phys. Chem. B,* 2004, **108,** 14340-14347.
[104] P. E. Batson, *Phys. Rev. B,* 1993, **48,** 2608-2610.
[105] J. Stöhr, *NEXAFS Spectroscopy*, Springer, Berlin, 1992.
[106] A. P. Hitchcock and I. Ishii, *J. Electron Spectrosc. Relat. Phenom.,* 1987, **42,** 11-26.
[107] A. P. Hitchcock, S. Beaulieu, T. Steel, J. Stöhr and F. Stette, *J. Chem. Phys.,* 1984, **80,** 3927-3935.
[108] G. Comelli, J. Stöhr, C. J. Robinson and W. Jark, *Phys. Rev. B,* 1988, **38,** 7511-7519.
[109] X. Li, K. Nagaoka, L. J. Simon, R. Olindo, J. A. Lercher, A. Hofmann and J. Sauer, *J. Am. Chem. Soc.,* 2005, **127,** 16159-16166.
[110] http://webbook.nist.gov/
[111] B. S. Klose, F. C. Jentoft, R. Schlögl, I. R. Subbotina and V. B. Kazansky, Langmuir 2005, 21, 10564–10572.
[112] F. C. Jentoft, A. Hahn, J. Kröhnert, G. Lorenz, R. E. Jentoft, T. Ressler, U. Wild and R. Schlögl, J. Catal. 2004, 224, 124–137.
[113] B. S. Klose, F. C. Jentoft, P. Joshi, A. Trunschke, R. Schlögl, I. R. Subbotina and V. B. Kazansky, Catal. Today 2006, 116, 121–131.
[114] H. Matsuhashi, H. Shibata, H. Nakamura and K. Arata, *Appl. Catal., A,* 1999, **187,** 99-106.
[115] V. Adeeva, G. D. Lei and W. M. H. Sachtler, *Catal. Lett.,* 1995, **33,** 135-143.
[116] F. Garin, L. Seyfried, P. Girard, G. Maire, A. Abdulsamad and J. Sommer, *J. Catal.,* 1995, **151,** 26-32.
[117] T. Echizen, T. Suzuki, Y. Kamiya and T. Okuhara, *J. Mol. Catal. A: Chem.,* 2004, **209,** 145-153.
[118] E. García, M. A. Volpe, M. L. Ferreira and E. Rueda, *J. Mol. Catal. A: Chem.,* 2003, **201,** 263-281.
[119] M. V. Luzgin, S. S. Arzumanov, V. P. Shmachkova, N. S. Kotsarenko, V. A. Rogov and A. G. Stepanov, *J. Catal.,* 2003, **220,** 233-239.
[120] V. Adeeva, H.-Y. Liu, B.-Q. Xu and W. M. H. Sachtler, *Top. Catal.,* 1998, **6,** 61-76.
[121] H. Liu, V. Adeeva, G. D. Lei and W. M. H. Sachtler, *J. Mol. Catal. A: Chem.,* 1995, **100,** 35-48.
[122] S. Y. Kim, J. G. Goodwin and D. Fărcaşiu, *Appl. Catal., A,* 2001, **207,** 281-286.
[123] R. Ahmad, J. Melsheimer, F. C. Jentoft and R. Schlögl, *J. Catal.,* 2003, 218, 365-374.
[124] X. Li, K. Nagaoka, L. J. Simon, R. Olindo and J. A. Lercher, *J. Catal.,* 2005, **232,** 456-466.